Design constraints of optical parametric chirped pulse amplification based on chirped quasi-phase-matching gratings

C. R. Phillips,[1,2,*] B. W. Mayer,[1] L. Gallmann,[1,3] M. M. Fejer,[2] and U. Keller[1]

[1]*Department of Physics, Institute of Quantum Electronics, ETH Zurich, 8093 Zurich, Switzerland*

[2]*Edward L. Ginzton Laboratory, Stanford University, Stanford, California 94305,USA*

[3]*Institute of Applied Physics, University of Bern, 3012 Bern, Switzerland*

[*]*cphillips@phys.ethz.ch*

Abstract: Chirped quasi-phase-matching (QPM) gratings offer efficient, ultra-broadband optical parametric chirped pulse amplification (OPCPA) in the mid-infrared as well as other spectral regions. Only recently, however, has this potential begun to be realized [1]. In this paper, we study the design of chirped QPM-based OPCPA in detail, revealing several important constraints which must be accounted for in order to obtain broad-band, high-quality amplification. We determine these constraints in terms of the underlying saturated nonlinear processes, and explain how they were met when designing our mid-IR OPCPA system. The issues considered include gain and saturation based on the basic three-wave mixing equations; suppression of unwanted non-collinear gain-guided modes; minimizing and characterizing nonlinear losses associated with random duty cycle errors in the QPM grating; avoiding coincidentally-phase-matched nonlinear processes; and controlling the temporal/spectral characteristics of the saturated nonlinear interaction in order to maintain the chirped-pulse structure required for OPCPA. The issues considered place constraints both on the QPM devices as well as the OPCPA system. The resulting experimental guidelines are detailed. Our results represent the first comprehensive discussion of chirped QPM devices operated in strongly nonlinear regimes, and provide a roadmap for advancing and experimentally implementing OPCPA systems based on these devices.

OCIS codes: (190.4970) Parametric oscillators and amplifiers; (190.4975) Parametric processes; (190.4420) Nonlinear optics, transverse effects in; (190.4360) Nonlinear optics, devices; (320.7110) Ultrafast nonlinear optics.

References and links

1. B. W. Mayer, C. R. Phillips, L. Gallmann, M. M. Fejer, and U. Keller, "Sub-four-cycle laser pulses directly from a high-repetition-rate optical parametric chirped-pulse amplifier at 3.4 μm," Opt. Lett. **38**, 4265–4268 (2013).
2. M. Charbonneau-Lefort, B. Afeyan, and M. M. Fejer, "Optical parametric amplifiers using chirped quasi-phase-matching gratings I: practical design formulas," J. Opt. Soc. Am. B **25**, 463–480 (2008).
3. M. Charbonneau-Lefort, B. Afeyan, and M. M. Fejer, "Competing collinear and noncollinear interactions in chirped quasi-phase-matched optical parametric amplifiers," J. Opt. Soc. Am. B **25**, 1402–1413 (2008).
4. C. Heese, C. R. Phillips, L. Gallmann, M. M. Fejer, and U. Keller, "Ultrabroadband, highly flexible amplifier for ultrashort midinfrared laser pulses based on aperiodically poled Mg:$LiNbO_3$," Opt. Lett. **35**, 2340–2342 (2010).

#205795 - $15.00 USD Received 4 Feb 2014; revised 3 Apr 2014; accepted 8 Apr 2014; published 15 Apr 2014

5. C. Heese, C. R. Phillips, B. W. Mayer, L. Gallmann, M. M. Fejer, and U. Keller, "75 MW few-cycle mid-infrared pulses from a collinear apodized APPLN-based OPCPA," Opt. Express **20**, 26888–26894 (2012).
6. C. R. Phillips and M. M. Fejer, "Efficiency and phase of optical parametric amplification in chirped quasi-phase-matched gratings," Opt. Lett. **35**, 3093–3095 (2010).
7. H. Suchowski, V. Prabhudesai, D. Oron, A. Arie, and Y. Silberberg, "Robust adiabatic sum frequency conversion," Opt. Express **17**, 12731–12740 (2009).
8. C. R. Phillips, C. Langrock, D. Chang, Y. W. Lin, L. Gallmann, and M. M. Fejer, "Apodization of chirped quasi-phasematching devices," J. Opt. Soc. Am. B **30**, 1551–1568 (2013).
9. G. Porat and A. Arie, "Efficient, broadband, and robust frequency conversion by fully nonlinear adiabatic three-wave mixing," J. Opt. Soc. Am. B **30**, 1342–1351 (2013).
10. O. Yaakobi, M. Clerici, L. Caspani, F. Vidal, and R. Morandotti, "Complete pump depletion by autoresonant second harmonic generation in a nonuniform medium," J. Opt. Soc. Am. B **30**, 1637–1642 (2013).
11. H. Suchowski, P. R. Krogen, S.-W. Huang, F. X. Kärtner, and J. Moses, "Octave-spanning coherent mid-IR generation via adiabatic difference frequency conversion," Opt. Express **21**, 28892-28901 (2013).
12. C. R. Phillips, L. Gallmann, and M. M. Fejer, "Design of quasi-phasematching gratings via convex optimization," Opt. Express **21**, 10139–10159 (2013).
13. K. A. Tillman, D. T. Reid, D. Artigas, J. Hellström, V. Pasiskevicius, and F. Laurell, "Low-threshold femtosecond optical parametric oscillator based on chirped-pulse frequency conversion," Opt. Lett. **28**, 543–545 (2003).
14. K. A. Tillman and D. T. Reid, "Monolithic optical parametric oscillator using chirped quasi-phase matching," Opt. Lett. **32**, 1548–1550 (2007).
15. L. Gallmann, G. Steinmeyer, U. Keller, G. Imeshev, M. M. Fejer, and J. Meyn, "Generation of sub-6-fs blue pulses by frequency doubling with quasi-phase-matching gratings," Opt. Lett. **26**, 614–616 (2001).
16. G. Imeshev, M. M. Fejer, A. Galvanauskas, and D. Harter, "Pulse shaping by difference-frequency mixing with quasi-phase-matching gratings," J. Opt. Soc. Am. B **18**, 534–539 (2001).
17. D. Artigas and D. T. Reid, "Efficient femtosecond optical parametric oscillators based on aperiodically poled nonlinear crystals," Opt. Lett. **27**, 851–853 (2002).
18. Y. Deng, A. Schwarz, H. Fattahi, M. Ueffing, X. Gu, M. Ossiander, T. Metzger, V. Pervak, H. Ishizuki, T. Taira, T. Kobayashi, G. Marcus, F. Krausz, R. Kienberger, and N. Karpowicz, "Carrier-envelope-phase-stable, 1.2 mJ, 1.5 cycle laser pulses at 2.1 μm," Opt. Lett. **37**, 4973–4975 (2012).
19. M. Conforti, F. Baronio, and C. D. Angelis, "From femtosecond infrared to picosecond visible pulses: temporal shaping with high-efficiency conversion," Opt. Lett. **32**, 1779–1781 (2007).
20. Ł. Kornaszewski, M. Kohler, U. K. Sapaev, and D. T. Reid, "Designer femtosecond pulse shaping using grating-engineered quasi-phase-matching in lithium niobate," Opt. Lett. **33**, 378–380 (2008).
21. C. Langrock, M. M. Fejer, I. Hartl, and M. E. Fermann, "Generation of octave-spanning spectra inside reverse-proton-exchanged periodically poled lithium niobate waveguides," Opt. Lett. **32**, 2478–2480 (2007).
22. T. W. Neely, L. Nugent-Glandorf, F. Adler, and S. A. Diddams, "Broadband mid-infrared frequency upconversion and spectroscopy with an aperiodically poled $LiNbO_3$ waveguide," Opt. Lett. **37**, 4332–4334 (2012).
23. V. J. Hernandez, C. V. Bennett, B. D. Moran, A. D. Drobshoff, D. Chang, C. Langrock, M. M. Fejer, and M. Ibsen, "104 MHz rate single-shot recording with subpicosecond resolution using temporal imaging," Opt. Express **21**, 196–203 (2013).
24. T. Umeki, M. Asobe, Y. Nishida, O. Tadanaga, K. Magari, T. Yanagawa, and H. Suzuki, "Widely tunable 3.4 μm band difference frequency generation using apodized $\chi^{(2)}$ grating," Opt. Lett. **32**, 1129–1131 (2007).
25. A. Bostani, A. Tehranchi, and R. Kashyap, "Engineering of effective second-order nonlinearity in uniform and chirped gratings," J. Opt. Soc. Am. B **29**, 2929–2934 (2012).
26. A. Shirakawa, I. Sakane, M. Takasaka, and T. Kobayashi, "Sub-5-fs visible pulse generation by pulse-front-matched noncollinear optical parametric amplification," Appl. Phys. Lett. **74**, 2268–2270 (1999).
27. D. Herrmann, L. Veisz, R. Tautz, F. Tavella, K. Schmid, V. Pervak, and F. Krausz, "Generation of sub-three-cycle, 16 TW light pulses by using noncollinear optical parametric chirped-pulse amplification," Opt. Lett. **34**, 2459–2461 (2009).
28. B. E. Schmidt, A. D. Shiner, P. Lassonde, J.-C. Kieffer, P. B. Corkum, D. M. Villeneuve, and F. Légaré, "CEP stable 1.6 cycle laser pulses at 1.8 μm," Opt. Express **19**, 6858–6864 (2011).
29. G. Andriukaitis, T. Balciunas, S. Aliauskas, A. Puglys, A. Baltuka, T. Popmintchev, M. Chen, M. M. Murnane, and H. C. Kapteyn, "90 GW peak power few-cycle mid-infrared pulses from an optical parametric amplifier," Opt. Lett. **36**, 2755–2757 (2011).
30. C. Li, D. Wang, L. Song, J. Liu, P. Liu, C. Xu, Y. Leng, R. Li, and Z. Xu, "Generation of carrier-envelope phase stabilized intense 1.5 cycle pulses at 1.75 μm," Opt. Express **19**, 6783–6789 (2011).
31. J. Rothhardt, S. Demmler, S. Hädrich, J. Limpert, and A. Tünnermann, "Octave-spanning OPCPA system delivering CEP-stable few-cycle pulses and 22 W of average power at 1 MHz repetition rate," Opt. Express **20**, 10870–10878 (2012).
32. S. Witte and K. Eikema, "Ultrafast optical parametric chirped-pulse amplification," Selected Topics in IEEE J. Quant. Electron. **18**, 296–307 (2012).
33. G. Cerullo and S. De Silvestri, "Ultrafast optical parametric amplifiers," Review of Scientific Instruments **74**,

#205795 - $15.00 USD Received 4 Feb 2014; revised 3 Apr 2014; accepted 8 Apr 2014; published 15 Apr 2014

1–18 (2003).
34. F. Krausz and M. Ivanov, "Attosecond physics," Rev. Mod. Phys. **81**, 163–234 (2009).
35. P. Colosimo, G. Doumy, C. I. Blaga, J. Wheeler, C. Hauri, F. Catoire, J. Tate, R. Chirla, A. M. March, G. G. Paulus, H. G. Muller, P. Agostini, and L. F. DiMauro, "Scaling strong-field interactions towards the classical limit," Nature Physics **4**, 386–389 (2008).
36. A. Cavalieri, N. Müller, T. Uphues, V. Yakovlev, A. Baltuška, B. Horvath, B. Schmidt, L. Blümel, R. Holzwarth, S. Hendel, M. Drescher, U. Kleineberg, P. M. Echenique, R. Kienberger, F. Krausz, and U. Heinzmann, "Attosecond spectroscopy in condensed matter," Nature **449**, 1029–1032 (2007).
37. A. N. Pfeiffer, C. Cirelli, M. Smolarski, D. Dimitrovski, M. Abu-Samha, L. B. Madsen, and U. Keller, "Attoclock reveals natural coordinates of the laser-induced tunnelling current flow in atoms," Nature Physics **8**, 76–80 (2011).
38. T. Rohwer, S. Hellmann, M. Wiesenmayer, C. Sohrt, A. Stange, B. Slomski, A. Carr, Y. Liu, L. M. Avila, M. Kalläne *et al.*, "Collapse of long-range charge order tracked by time-resolved photoemission at high momenta," Nature **471**, 490–493 (2011).
39. C. T. Middleton, P. Marek, P. Cao, C.-c. Chiu, S. Singh, A. M. Woys, J. J. de Pablo, D. P. Raleigh, and M. T. Zanni, "Two-dimensional infrared spectroscopy reveals the complex behaviour of an amyloid fibril inhibitor," Nature chemistry **4**, 355–360 (2012).
40. T. Popmintchev, M.-C. Chen, D. Popmintchev, P. Arpin, S. Brown, S. Alisauskas, G. Andriukaitis, T. Balciunas, O. D. Mcke, A. Pugzlys, A. Baltuska, B. Shim, S. E. Schrauth, A. Gaeta, C. Hernndez-Garca, L. Plaja, A. Becker, A. Jaron-Becker, M. M. Murnane, and H. C. Kapteyn, "Bright coherent ultrahigh harmonics in the keV X-ray regime from mid-infrared femtosecond lasers," Science **336**, 1287–1291 (2012).
41. P. Russbueldt, T. Mans, J. Weitenberg, H. D. Hoffmann, and R. Poprawe, "Compact diode-pumped 1.1 kW Yb:YAG Innoslab femtosecond amplifier," Opt. Lett. **35**, 4169–4171 (2010).
42. T. Eidam, S. Hanf, E. Seise, T. V. Andersen, T. Gabler, C. Wirth, T. Schreiber, J. Limpert, and A. Tünnermann, "Femtosecond fiber CPA system emitting 830 w average output power," Opt. Lett. **35**, 94–96 (2010).
43. C. Heese, C. R. Phillips, L. Gallmann, M. M. Fejer, and U. Keller, "Role of apodization in optical parametric amplifiers based on aperiodic quasi-phasematching gratings," Opt. Express **20**, 18066–18071 (2012).
44. C. Heese, A. E. Oehler, L. Gallmann, and U. Keller, "High-energy picosecond Nd:YVO4 slab amplifier for OPCPA pumping," Applied Physics B **103**, 5–8 (2011).
45. M. Conforti, F. Baronio, and C. De Angelis, "Nonlinear envelope equation for broadband optical pulses in quadratic media," Physical Review A **81**, 053841 (2010).
46. C. R. Phillips, C. Langrock, J. S. Pelc, M. M. Fejer, I. Hartl, and M. E. Fermann, "Supercontinuum generation in quasi-phasematched waveguides," Opt. Express **19**, 18754–18773 (2011).
47. D. T. Reid, "Ultra-broadband pulse evolution in optical parametric oscillators," Opt. Express **19**, 17979–17984 (2011).
48. C. R. Phillips, C. Langrock, J. S. Pelc, M. M. Fejer, J. Jiang, M. E. Fermann, and I. Hartl, "Supercontinuum generation in quasi-phase-matched $LiNbO_3$ waveguide pumped by a Tm-doped fiber laser system," Opt. Lett. **36**, 3912–3914 (2011).
49. M. Kolesik and J. V. Moloney, "Nonlinear optical pulse propagation simulation: from maxwell's to unidirectional equations," Physical Review. E **70**, 036604 (2004).
50. C. R. Phillips, J. S. Pelc, and M. M. Fejer, "Parametric processes in quasi-phasematching gratings with random duty cycle errors," J. Opt. Soc. Am. B **30**, 982–993 (2013).
51. R. A. Baumgartner and R. Byer, "Optical parametric amplification," Quantum Electronics, IEEE Journal of **15**, 432–444 (1979).
52. M. Charbonneau-Lefort, B. Afeyan, and M. M. Fejer, "Theory and simulation of gain-guided noncollinear modes in chirped quasi-phase-matched optical parametric amplifiers," J. Opt. Soc. Am. B **27**, 824–841 (2010).
53. O. Gayer, Z. Sacks, E. Galun, and A. Arie, "Temperature and wavelength dependent refractive index equations for MgO-doped congruent and stoichiometric $LiNbO_3$," Appl. Phys. B: Lasers Opt. **91**, 343–348 (2008).
54. I. Shoji, T. Kondo, A. Kitamoto, M. Shirane, and R. Ito, "Absolute scale of second-order nonlinear-optical coefficients," J. Opt. Soc. Am. B **14**, 2268–2294 (1997).
55. R. DeSalvo, A. Said, D. Hagan, E. Van Stryland, and M. Sheik-Bahae, "Infrared to ultraviolet measurements of two-photon absorption and n_2 in wide bandgap solids," IEEE J. Quant. Electron. **32**, 1324–1333 (1996).
56. O. Beyer, D. Maxein, K. Buse, B. Sturman, H. T. Hsieh, and D. Psaltis, "Investigation of nonlinear absorption processes with femtosecond light pulses in lithium niobate crystals," Phys. Rev. E **71**, 056603 (2005).
57. P. Reckenthaeler, D. Maxein, T. Woike, K. Buse, and B. Sturman, "Separation of optical Kerr and free-carrier nonlinear responses with femtosecond light pulses in $LiNbO_3$ crystals," Physical Review B **76**, 195117 (2007).
58. J. R. Schwesyg, M. Falk, C. R. Phillips, D. H. Jundt, K. Buse, and M. M. Fejer, "Pyroelectrically induced photorefractive damage in magnesium-doped lithium niobate crystals," J. Opt. Soc. Am. B **28**, 1973–1987 (2011).
59. M. Charbonneau-Lefort, B. Afeyan, and M. M. Fejer, "Optical parametric amplifiers using nonuniform quasi-phase-matched gratings. II. space-time evolution of light pulses," J. Opt. Soc. Am. B **25**, 683–700 (2008).
60. R. Schiek, "Nonlinear refraction caused by cascaded second-order nonlinearity in optical waveguide structures," J. Opt. Soc. Am. B **10**, 1848–1855 (1993).

#205795 - $15.00 USD Received 4 Feb 2014; revised 3 Apr 2014; accepted 8 Apr 2014; published 15 Apr 2014

61. H. Ishizuki and T. Taira, "Half-joule output optical-parametric oscillation by using 10-mm-thick periodically poled mg-doped congruent linbo3," Opt. Express **20**, 20002–20010 (2012).
62. D. S. Hum, R. K. Route, and M. M. Fejer, "Quasi-phase-matched second-harmonic generation of 532 nm radiation in 25°-rotated, x-cut, near-stoichiometric, lithium tantalate fabricated by vapor transport equilibration," Opt. Lett. **32**, 961–963 (2007).
63. F. Druon, M. Hanna, G. Lucas-Leclin, Y. Zaouter, D. Papadopoulos, and P. Georges, "Simple and general method to calculate the dispersion properties of complex and aberrated stretchers-compressors," J. Opt. Soc. Am. B **25**, 754–762 (2008).
64. M. Charbonneau-Lefort, M. M. Fejer, and B. Afeyan, "Tandem chirped quasi-phase-matching grating optical parametric amplifier design for simultaneous group delay and gain control," Opt. Lett. **30**, 634–636 (2005).
65. C. Lynch, D. Bliss, T. Zens, A. Lin, J. Harris, P. Kuo, and M. Fejer, "Growth of mm-thick orientation-patterned GaAs for IR and THz generation," Journal of Crystal Growth **310**, 5241–5247 (2008).
66. C. R. Phillips, J. Jiang, C. Mohr, A. C. Lin, C. Langrock, M. Snure, D. Bliss, M. Zhu, I. Hartl, J. S. Harris, M. E. Fermann, and M. M. Fejer, "Widely tunable midinfrared difference frequency generation in orientation-patterned gaas pumped with a femtosecond tm-fiber system," Opt. Lett. **37**, 2928–2930 (2012).
67. J. Kiessling, R. Sowade, I. Breunig, K. Buse, and V. Dierolf, "Cascaded optical parametric oscillations generating tunable terahertz waves in periodically poled lithium niobate crystals," Opt. Express **17**, 87–91 (2009).
68. R. Sowade, I. Breunig, I. Camara Mayorga, J. Kiessling, C. Tulea, V. Dierolf, and K. Buse, "Continuous-wave optical parametric terahertz source," Opt. Express **17**, 22303 (2009).
69. C. R. Phillips, J. S. Pelc, and M. M. Fejer, "Continuous wave monolithic quasi-phase-matched optical parametric oscillator in periodically poled lithium niobate," Opt. Lett. **36**, 2973–2975 (2011).
70. C. R. Phillips and M. M. Fejer, "Adiabatic optical parametric oscillators: steady-state and dynamical behavior," Opt. Express **20**, 2466–2482 (2012).
71. K. Vodopyanov, "Optical THz-wave generation with periodically-inverted GaAs," Laser & Photonics Reviews **2**, 11–25 (2008).
72. H. Jang, G. Strömqvist, V. Pasiskevicius, and C. Canalias, "Control of forward stimulated polariton scattering in periodically-poled KTP crystals," Opt. Express **21**, 27277–27283 (2013).

1. Introduction

Quasi-phase-matching (QPM) has been an enabling technology for many frequency conversion schemes and their applications. An important advantage of QPM over conventional birefringent phase-matching (BPM) is the additional capability to design frequency converters having desired properties, such as a broad bandwidth with a custom amplitude or phase profile, while still utilizing the largest nonlinear coefficient of the QPM material. Such capabilities have been made possible by lithographic fabrication techniques, which enable accurate construction of non-uniform QPM gratings containing a wide range of spatial frequency content. Chirped QPM gratings, in which the grating k-vector is varied smoothly and monotonically through the length of the device, have proven to be particularly useful in ultrafast optics, since the corresponding phase-matching bandwidth can be made almost arbitrarily large while maintaining a smooth spectral phase profile.

Chirped QPM gratings have been widely deployed in frequency conversion schemes involving second-harmonic generation (SHG), difference frequency generation (DFG), sum frequency generation (SFG), optical parametric oscillators (OPOs), and related applications [1–25]. Their main role historically has been to broaden the phase-matching bandwidth compared to conventional periodic QPM gratings, without the need to use short crystals with reduced conversion efficiency, tighter focusing, higher intensities, operation close to the damage threshold, or other potential drawbacks. Quite recently, new applications of chirped QPM gratings have emerged, in particular high-gain optical parametric amplification (OPA) [1–6], and high-efficiency adiabatic frequency conversion (AFC) [6–11]. Together, these processes reveal the possibility of achieving essentially arbitrary-bandwidth, high-efficiency optical parametric chirped pulse amplification (OPCPA) within the transparency window of QPM media, while simultaneously suppressing gain-narrowing effects [12]. Such an approach is an important tool for OPA and OPCPA development [1,18,26–33], as well as for the emergent field of attosecond science [34–40], offering high-intensity few-cycle pulse generation at high repetition rates and

#205795 - $15.00 USD Received 4 Feb 2014; revised 3 Apr 2014; accepted 8 Apr 2014; published 15 Apr 2014

in new wavelength regions from comparatively simple and collinear experimental geometries, utilizing power-scalable 1-μm pump lasers [41, 42]. This potential has motivated the development of our mid-IR OPCPA system, which has most recently enabled generation of sub-four-cycle pulses in the mid-IR directly from the OPCPA output [1].

While obtaining arbitrary phase-matching bandwidth is a relatively straightforward process of fabricating a structure with the required range of QPM periods, achieving high-quality ultra-broadband OPA or OPCPA is much more challenging, owing in particular to subtle additional effects which emerge due to the high intensities and strongly nonlinear interactions involved. Indeed, broadband operation in this case requires careful control of the ultrafast dynamics of a nonlinear, spatially inhomogeneous medium. Understanding and manipulating the associated physical processes is very important for the continued advancement of such devices.

In this paper, we examine in detail several nonlinear processes which occur in high-gain and strongly-saturated QPM interactions, and thereby determine the design constraints which must be met by OPCPA systems based on chirped QPM devices to avoid such effects while still supporting broad bandwidths and good conversion efficiency. Throughout the paper, we discuss these constraints in the context of our high repetition rate mid-IR OPCPA system, in particular to explain how we arrived at our most recent OPCPA result [1], which yielded almost a factor of 2 shorter pulse duration compared to our result from a year earlier [5, 43], and promises further improvements in the near future. The physics, design constraints, and system design procedures we develop will be applicable to OPCPA, AFC interactions, and to strongly nonlinear parametric systems in general, especially those involving spatially inhomogeneous phase-matching media.

The paper is arranged as follows. In section 2, we introduce the experimental OPCPA setup reported in [1], explaining its characteristic features. In section 3, we show the fundamental properties of OPA and AFC in chirped QPM devices, as well as corresponding OPCPA design guidelines. In section 4, we discuss transverse beam effects, in particular the existence of gain-guided modes and their suppression in the context of OPCPA. In section 5, we consider random duty cycle (RDC) errors in QPM structures, and the role these imperfections can have on OPCPA performance. In section 6, we examine additional, unwanted mixing processes supported by the $\chi^{(2)}$ nonlinearity, and show how these can be suppressed. In section 7, we describe the effects of group velocity mismatch on saturated chirped-QPM interactions, and the corresponding implications for pulse chirping in order to avoid deleterious effects. With the analysis from the above sections in hand, in section 8 we collect the key OPCPA design constraints, further explain their implications and application to the mid-IR OPCPA system described in section 2, and discuss the results. In appendix B, we provide for convenience a summary of the definitions used in the paper.

2. Experimental system

In this section, we give a brief description of the mid-IR OPCPA system described Ref. [1], in order to motivate and give context to the OPCPA design study performed in this paper. Our system is shown schematically in Fig. 1.

The primary seed laser for the system is a 1.56-μm femtosecond fiber laser (Toptica FFS) which produces 65-fs pulses at 80 MHz and an average power of 250 mW (3.1 nJ). We spectrally broaden this source using a dispersion-shifted telecom fiber (Thorlabs DCF3) to provide $>$ 200-nm bandwidth (corresponding to $>$1000-nm bandwidth for the 3.4-μm idler), before chirping to few-ps durations via a pair of silicon prisms and a 4f pulse shaper in order to provide a suitable OPCPA seed. This chirping configuration was chosen with compression of the final 3.4-μm idler output of the OPCPA chain in mind. The seed energy reaching the OPCPA chain is 92.5 pJ. The primary pump laser is a 1.064-μm industrial laser (Time-Bandwidth Prod-

#205795 - $15.00 USD Received 4 Feb 2014; revised 3 Apr 2014; accepted 8 Apr 2014; published 15 Apr 2014

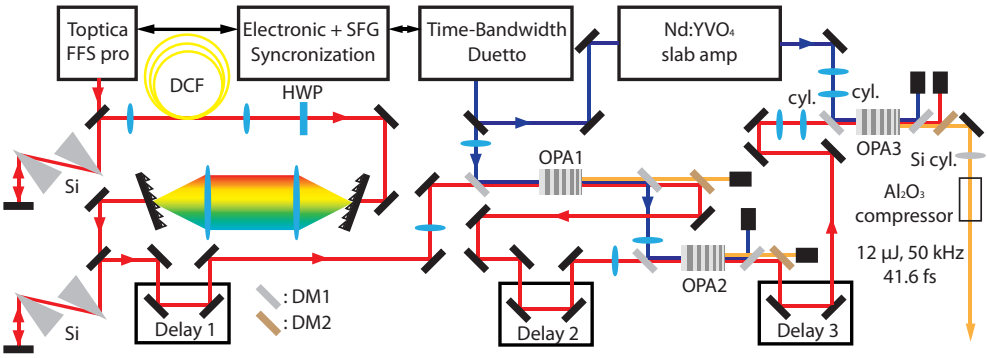

Fig. 1. Schematic overview of the mid-infrared OPCPA setup. DM: dichroic mirrors. DM1: reflective 1064 nm / transmissive 1560 nm & 3400 nm, DM2: reflective 1560 nm / transmissive 3400 nm. The OPA2 and OPA3 amplification stages are seeded by the 1560-nm signal output beams from OPA1 and OPA2, respectively; the 3400-nm idler output beams from OPA1 and OPA2 are discarded. For OPA3, the signal output is discarded, and the idler output is compressed in a bulk sapphire rod.

ucts Duetto) which can produce 12-ps pulses at 50 kHz and an average power of up to 10 W. We split these pulses into two parts, and further amplify one part in a home-built amplifier [44], based on the Innoslab concept [41]. This amplification yields 15.2 W (304 μJ) of power immediately before the final OPA stage, denoted OPA3.

The OPCPA chain consists of three aperiodically poled (i.e. chirped) MgO:$LiNbO_3$ gratings (denoted APPLN), each having the same apodized and chirped grating design [8]; the gratings are 11-mm-long, 1-mm-thick, and 3-mm-wide, with a chirp rate of $\Delta k' = -2.5$ mm^{-2} in order to achieve a broad phase-matching bandwidth spanning the 3- to 4-μm spectral range. All stages are operated in a collinear beam geometry. The first two OPA stages (denoted OPA1 and OPA2) are pumped by the residual Duetto output of 5.7 W (the part not used to seed the Innoslab amplifier). The transmitted pump from OPA1 is used to pump OPA2, so as to maximize the peak power in both stages given the available power. OPA3 is pumped by the output of the Innoslab amplifier. The OPCPA chain is seeded by the signal wave at 1.56-μm, and the amplified signal is propagated through the system until the final OPA stage, after which we extract and compress the collinearly-generated 3.4-μm idler wave. The idler is compressed by low-loss bulk propagation through 50 mm of AR-coated sapphire. These design choices are explained in sections 3-7, and the various constraints are summarized in subsection 8.1. A more detailed account of the experimental setup and results is given in [1].

The compressed idler pulses have a duration of 41.6 fs and an energy of 12 μJ, at a repetition rate of 50 kHz. We currently use uncoated APPLN samples; accounting for these and other linear losses, we estimate an energy of 19 μJ inside OPA3, which represents a reasonable quantum conversion efficiency of 24.5% in the final stage. The study we perform in the following sections explains our improved system layout and design, the limiting factors in terms of OPCPA physics, and points the way towards further improvements in pulse duration and energy.

3. OPCPA in chirped QPM gratings

In this section, we introduce the fundamental properties of chirped QPM gratings for OPCPA. In subsection 3.1, we introduce general coupled-wave equations which will be used later as the starting point to establish several system design constraints. In subsection 3.2 we recapitulate the interaction between plane- and continuous-wave (cw) pump, signal, and idler fields in the

#205795 - $15.00 USD Received 4 Feb 2014; revised 3 Apr 2014; accepted 8 Apr 2014; published 15 Apr 2014

chirped QPM OPA regime. In subsection 3.3, we discuss pump depletion (saturation) in this regime, and corresponding implications for OPCPA system layout. The paper involves various definitions and symbols: for convenience, these are summarized in appendix B.

3.1. Coupled-envelope equations

OPCPA ideally involves the interaction between individual signal and idler frequency components, and a corresponding region of the pump pulse in the time domain. However, other mixing processes are possible and can perturb the desired interaction. In recent years, general single-envelope descriptions of $\chi^{(2)}$ mixing processes have emerged that account for all of the interactions between co-propagating waves [45–47]. In Ref. [46], interactions in QPM waveguides were considered, accounting for both $\chi^{(2)}$ and $\chi^{(3)}$ processes in a general frequency-domain approach for the first time; all orders of QPM, multiple waveguide modes (with a single envelope used to describe the spectrum of each mode), and a re-calibration of the $\chi^{(3)}$ coefficients (both instantaneous and Raman nonlinearities) were included. We found that this level of generality was needed to accurately model previous supercontinuum generation results [46, 48].

In the case of OPCPA, the chirped structure of the pulses involved means that even for very broad bandwidths, the electric field can be split up naturally into multiple envelopes. Here, we present a multiple-envelope model allowing for any number of additional envelopes corresponding to various sum and difference frequency mixing between the signal, idler and pump envelopes. By accounting for all the possible mixing processes between these envelopes, the resulting dynamics can be captured with generality comparable to single-envelope techniques, but with the advantage of clearly modelling and isolating the important processes involved, and without the need to resolve the optical carrier frequency.

Building on the frequency-domain approach of Ref. [46] and the general formalism which has been shown for unidirectional wave propagation problems as an important extension of conventional slowly-varying envelope approximations [49], we arrive at a set of coupled-envelope equations describing the extraordinary-wave (*e*-wave) polarization components of the electric field in the nonlinear crystal, assuming paraxial and collinear beams and a uniaxial crystal:

$$\frac{\partial \tilde{A}_j(\omega-\omega_j)}{\partial z}+\hat{L}_j(\omega)\tilde{A}_j(\omega-\omega_j)=-i\frac{\omega^2 u(\omega)}{k_e(\omega)c^2\varepsilon_0}\mathscr{F}\left[P_{NL,j}\right](\omega-\omega_j). \tag{1}$$

In this equation, coordinate z represents the propagation direction and x is along the c-axis of the crystal. k_o and k_e denote the frequency-dependent propagation constants for the *o*- and *e*-wave polarizations. The field envelope for wave j is denoted A_j, and tilde's denoting frequency domain envelope quantities [46]. ω_j is the carrier frequency of wave j, and ω (lower-case) represents absolute optical frequencies. $P_{NL,j}$ is the nonlinear polarization driving wave j. $\mathscr{F}$ is the Fourier transform, defined as $\tilde{g}(\Omega)=\mathscr{F}[g(t)](\Omega)=\int_{-\infty}^{\infty}g(t)\exp(-i\Omega t)dt$. $\hat{L}_j$ denotes the (frequency-dependent) diffraction and dispersion operator for wave j, and is given by

$$\hat{L}_j(\omega)=\frac{i}{2}\left(\frac{k_e(\omega)}{k_o(\omega)^2}\frac{\partial^2}{\partial x^2}+\frac{1}{k_e(\omega)}\frac{\partial^2}{\partial y^2}\right)+i\left[k_e(\omega)-k_e(\omega_j)-\frac{\omega-\omega_j}{v_{ref}}\right]. \tag{2}$$

We use a moving coordinate system based on a reference group velocity v_{ref}, which is typically chosen to be a weighted average of the pump, signal, and idler group velocities. The total, real-valued electric field $E(x,y,z,t)$ can be expressed in terms of the envelopes A_j in the frequency domain according to

$$\tilde{E}(\omega)u(\omega)=\frac{1}{2}\sum_j\tilde{A}_j(\omega-\omega_j)e^{-ik_e(\omega_j)z}, \tag{3}$$

#205795 - $15.00 USD Received 4 Feb 2014; revised 3 Apr 2014; accepted 8 Apr 2014; published 15 Apr 2014

where $u(\omega)$ appearing in Eqs. (1) and (3) is the Heaviside step function; the form of these equations arises because we assume A_j are (shifted) analytic signals (i.e. spectral components equal to zero for *absolute* optical frequencies $\omega < 0$).

The nonlinear polarization for each wave is given by

$$\frac{P_{NL,j}(t)}{\varepsilon_0} = \frac{d_{33}}{2}\sum_{k,l}\sum_{m}\bar{d_m}\Bigg[\left(X_{j,kl}e^{+i(\Delta k_{j,kl}z - m\phi_G(z))}\right)A_k(t)A_l(t) + \left(2X_{k,jl}e^{-i(\Delta k_{j,kl}z - m\phi_G(z))}\right)A_k(t)A_l(t)^*\Bigg], \tag{4}$$

where this form accounts for all possible $\chi^{(2)}$ mixing processes between the envelopes included in the model, implicitly assuming an all-e-wave interaction for simplicity, that all other envelopes (corresponding to different sums and differences of the included carrier frequencies) are negligible, and that $\chi^{(2)}$ is non-dispersive. Note that dependencies of both the nonlinear polarization and the fields on spatial coordinates have been suppressed for compactness. The coefficients $X_{j,kl}$ specify which waves are coupled to each other according to energy conservation, and hence satisfy

$$X_{j,kl} = \begin{cases} 0, & \omega_j \neq \omega_k + \omega_l \\ 1, & \omega_j = \omega_k + \omega_l \end{cases}. \tag{5}$$

For numerical calculations, of course, terms with $X_{j,kl} = 0$ can be ignored, and duplicated terms can be calculated once and multiplied by two. The phase mismatches Δk appearing in Eq. (4) are given by

$$\Delta k_{j,kl} = k_e(\omega_j) - k_e(\omega_k) - k_e(\omega_l). \tag{6}$$

For a QPM interaction, we can express the spatially-varying nonlinear coefficient in terms of its Fourier orders, even for cases with an aperiodic grating. Following [50], $d(z)$ is given by

$$\frac{d(z)}{d_{33}} = \mathrm{sgn}\left[\cos(\phi_G(z)) - \cos(\pi D(z))\right] \equiv \bar{d_0}(z) + \sum_{\substack{m=-\infty \\ m\neq 0}}^{\infty}\bar{d_m}(z)\exp\left(im\phi_G(z)\right) \tag{7}$$

where m denotes the Fourier orders of the grating, the grating phase is $\phi_G(z) = \int_0^z K_g(z')dz'$ for local grating k-vector $K_g(z)$, d_{33} is the relevant nonlinear coefficient of the material for an all-e-wave interaction, and $D(z)$ is local grating duty cycle. The Fourier coefficients are given by $\bar{d_0} = (2D(z) - 1)$ and $\bar{d_m} = 2\sin(\pi m D(z))/(\pi m)$ for $m \neq 0$. Note that the signs of the $\pm[\Delta k_{j,kl}z - m\phi_G(z)]$ phases in Eq. (4) are needed in order to satisfy energy conservation for each of the individual interactions involved (i.e. a particular set of envelopes $\{j,k,l\}$ and a particular QPM order m). The coefficients $X_{j,kl}$ and the form of Eqs. (1) and (4) mean that all interactions involving only the envelopes included in the model are accounted for, and that the full system of equations conserves energy.

3.2. Quasi-cw mixing in the undepleted-pump regime

While Eq. (1) is very general, simplified sets of equations are also useful in order to gain insight into the processes involved. In this subsection, we model plane-wave and quasi-cw interactions between the three nominal envelopes (pump, signal, and idler), including only the first QPM

#205795 - $15.00 USD Received 4 Feb 2014; revised 3 Apr 2014; accepted 8 Apr 2014; published 15 Apr 2014

order. Under these approximations, Eq. (1) can be reduced to the following, more familiar set of coupled-wave equations [8]:

$$\frac{dA_{i,s}}{dz} = -i\frac{\omega_{i,s}\left(d_{33}\bar{d_1}\right)}{n_{i,s}c}A_pA^*_{s,i}\exp\left[-i\int_0^z \Delta\beta(z')dz'\right] \tag{8a}$$

$$\frac{dA_p}{dz} = -i\frac{\omega_p\left(d_{33}\bar{d_1}\right)}{n_pc}A_iA_s\exp\left[+i\int_0^z \Delta\beta(z')dz'\right], \tag{8b}$$

where $\Delta\beta = k_e(\omega_p) - k_e(\omega_s) - k_e(\omega_i) - K_g(z)$, and n_j denotes the refractive index of wave j. The effective first-order-QPM nonlinear coefficient is $d_{\text{eff}} = d_{33}\bar{d_1}$, where $\bar{d_1} = 2/\pi$ for a 50-% duty cycle grating.

Following [8], based on the coefficients in these equations, we can define coupling rates satisfying $\gamma_p^2 = (\omega_i\omega_s d_{33}^2\bar{d_1^2})/(n_in_sc^2)|A_p(z=0)|^2$ and $\gamma_s^2 = (\omega_i\omega_p d_{33}^2\bar{d_1^2})/(n_in_pc^2)|A_s(z=0)|^2$. From [2], the OPA power gain for the input signal wave in a long, linearly chirped grating assuming a strong and undepleted pump and zero input idler is given by

$$G_s = \exp\left(2\pi\frac{\gamma_p^2}{|\Delta k'|}\right) \tag{9}$$

where $\Delta k' = -dK_g/dz$ is the QPM chirp rate (the rate of change of the phase mismatch with respect to z).

For OPCPA, we must account for the time-dependent pump intensity and the temporal localization of signal and idler spectral components. In the limit of highly chirped pulses, there is a mapping between signal and idler frequencies and time, and hence pump intensity, resulting in gain narrowing effects. In this chirped-pulse limit, a frequency-dependent coupling rate between signal and idler fields can be defined to account for such effects. We explained this procedure in the context of chirped QPM OPCPA in [12], arriving at the following general expression for the frequency-dependent gain:

$$G_s(\Omega) \approx \exp\left[2\int_{z_{tp,1}(\Omega)}^{z_{tp,2}(\Omega)}\sqrt{\gamma_p(\Omega)^2 - \left(\frac{\Delta k_0(\Omega) - K_g(z)}{2}\right)^2}dz\right], \tag{10}$$

the form of which is reminiscent of the OPA gain rate in unchirped structures [51]. The frequency-dependent signal-idler coupling coefficient is given by

$$\gamma_p(\Omega)^2 = \frac{(\omega_i-\Omega)(\omega_s+\Omega)(\bar{d_1}d_{33})^2}{n_e(\omega_i-\Omega)n_e(\omega_s+\Omega)c^2}\frac{2}{n_e(\omega_p)\varepsilon_0 c}I_p(\tau_s(\omega_s+\Omega)), \tag{11}$$

$I_p(t)$ is the pump intensity, the single-frequency-argument material phase mismatch is given by

$$\Delta k_0(\Omega) = k_e(\omega_p) - k_e(\omega_s+\Omega) - k_e(\omega_i-\Omega), \tag{12}$$

$\tau_s(\omega_s+\Omega)$ denotes the delay at which signal frequency $\omega_s+\Omega$ is localized, and $z_{tp,j}(\Omega)$ denote the 'turning points' in Eq. (10), i.e. the points at which the integrand is zero. Since this integrand is the gain coefficient in an unchirped OPA device, these turning points represent the points where the local phase-mismatch is large enough that the OPA gain coefficient vanishes. Another important variable is $z_{pm}(\Omega)$, defined as frequency-dependent phase-matching point satisfying

$$\Delta k_0(\Omega) - K_g(z_{pm}(\Omega)) = 0. \tag{13}$$

#205795 - $15.00 USD Received 4 Feb 2014; revised 3 Apr 2014; accepted 8 Apr 2014; published 15 Apr 2014

Further insight into these quantities is given in Fig. 2, where we show an overview of chirped-QPM OPA interactions.

The form for the gain in Eq. (10) can be used to find globally optimal chirp profiles to obtain custom gain (and phase) spectra, as shown via a convex optimization framework in [12]. Here, we use simplified design criteria for this aspect of the problem, but the general procedures of [12] can be applied provided that the additional constraints we will discuss in this paper are addressed. An important property of Eq. (10), described in more detail in Ref. [2], is that gain takes place between the 'turning points' $z_{tp,1}(\Omega)$ and $z_{tp,2}(\Omega)$. For a linear chirp rate $\Delta k' = -dK_g/dz = \text{constant}$, there is a dephasing length, which is the distance required to go from perfect phase-matching ($\Delta k_0 - K_g = 0$) to zero amplification rate ($|\Delta k_0 - K_g| = 2\gamma_p$). This dephasing length is given by

$$L_{\text{deph}} = \frac{2\gamma_p}{|\Delta k'|}. \tag{14}$$

We can define an OPA bandwidth as the range of frequencies which experience complete amplification according to Eq. (10). Assuming for simplicity a linear, unapodized chirp profile and approximating $\gamma_p(\Omega) \approx \gamma_{p0}$ for peak coupling coefficient γ_{p0}, we find the following for the range of material phase mismatches that are fully amplified:

$$\begin{aligned} \Delta k_{\text{OPA}} &\approx |\Delta k'|L - 4\gamma_{p0} \\ &\equiv \Delta k_{BW} - 4\gamma_{p0}. \end{aligned} \tag{15}$$

In turn, the material dispersion determines the spread of the phase mismatch for a given pump wavelength and signal/idler spectral region of interest. Given a desired gain and bandwidth, Eqs. (9) and (15) can be used to determine the grating length L and chirp rate $\Delta k'$ required as a function of the coupling coefficient γ_{p0}. For any given nominal grating design, it is essential to also append apodization regions in order to obtain a useful gain spectrum, as discussed in [8].

The value of γ_{p0} is related to the peak intensity of the pump; a useful relation for the signal gain coefficient in terms of the pump peak power P_{pk}, confocal parameter ξ_p, and phase-matching bandwidth is

$$\Lambda_{R,p} \equiv \frac{\gamma_{p0}^2}{|\Delta k'|} = \frac{4\omega_i\omega_s\omega_p(\bar{d}_1 d_{33})^2}{\pi\varepsilon_0 c^4 n_i n_s} \frac{\xi_p P_{pk}}{|\Delta k'|L}. \tag{16}$$

where $\xi_p = L/(k_p w_p^2)$, $\Lambda_{R,p}$ is the peak gain factor, and Eq. (16) implicitly assumes a pump with $M^2 = 1$ and $1/e^2$ beam radius w_p. Equation (16) can provide intuition for some of the required experimental conditions for a given peak small-signal gain $G_s = \exp(2\pi\Lambda_{R,p})$, especially in cases where $\Delta k_{\text{OPA}} \approx |\Delta k'|L$ (although this latter approximation is not always accurate).

3.3. Quasi-cw mixing with saturation effects

Another important aspect of the problem is the effects of saturation. A key feature of chirped QPM devices is adiabatic frequency conversion (AFC) [6, 7], which in the context of OPA enables a conversion efficiency of the pump to the sum of the signal and idler which asymptotes to 100% with respect to both the pump and signal input intensities, provided that the chirp rate is sufficiently slow with respect to the coupling between the waves, and that the range of grating k-vectors is sufficiently large. AFC was recently studied in detail theoretically for the general nonlinear three-wave mixing cases [8, 9]. The essentially arbitrary conversion efficiencies predicted by simplified three-wave models is made challenging by several practical constraints such as limits on how strong the coupling between the fields can be made, as well as the onset of additional, unwanted processes. We discuss such processes in subsequent sections.

#205795 - $15.00 USD Received 4 Feb 2014; revised 3 Apr 2014; accepted 8 Apr 2014; published 15 Apr 2014

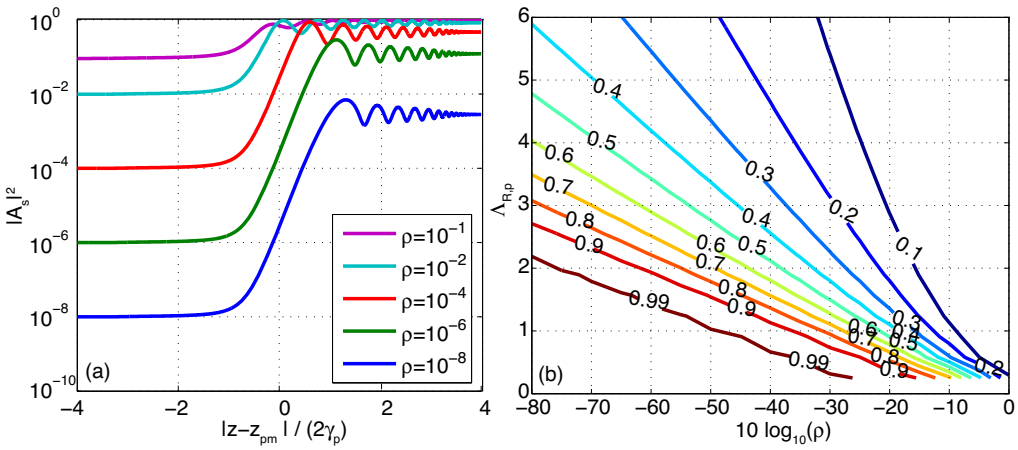

Fig. 2. (a) Example evolution of the three waves in a cw OPA interaction. For small ρ, the amplification corresponds closely to Eqs. (9) and (10). For larger ρ, the interaction approaches the adiabatic frequency conversion case [8, 9], and for $\rho \gg 1$ (corresponding to DFG or SFG rather than OPA), correspond to the case considered in [7]. The predicted conversion efficiency increases with both $\Lambda_{R,p}$ and ρ, as can be seen from (b). The turning points $z_{tp,j}$ appearing in Eq. (10) are the two points where the normalized position coordinate $(z-z_{pm})/(2\gamma_p) = \pm 1$: the $\rho = 10^{-8}$ curve in the figure clearly shows that the exponential gain takes place between these two points. Note also that z_{pm} is frequency dependent due to the dispersion of the material, so different wavelengths are amplified around different longitudinal positions. (b) Simulated pump depletion $\eta_p = |A_p(L)/A_p(0)|^2$ as a function of $\Lambda_{R,p}$ (which determines the small-signal OPA gain) and ρ (which denotes the ratio of input signal and pump photon fluxes, and hence how much gain is required in order to saturate the pump). Contours are labelled with values of η_p. The grating length is chosen such that $L \gg 2L_{\text{deph}}$ in each case [L_{deph} defined in Eq. (14)], and hence has L negligible impact on the pump depletion .

Important characteristic quantities of the three-wave mixing interaction [see Eqs. (8)] are $\Lambda_{R,p} = \gamma_p^2/|\Delta k'|$ and $\Lambda_{R,s} = \gamma_s^2/|\Delta k'|$, and $\rho = N_s(0)/N_p(0)$, where $N_j(z)$ denote the photon fluxes of wave j. It can be shown that $\Lambda_{R,s} = \rho\Lambda_{R,p}$. In the case of a strong signal and weak pump (i.e. $\Lambda_{R,s} > 1$ and $\rho \gg 1$), the pump depletion, defined as $\eta_p = |A_p(L)/A_p(0)|^2$, can be approximated as $\eta_p = \exp(-2\pi\Lambda_{R,s})$ [7].

For OPA, we will generally have $\Lambda_{R,p}$ of order unity. Therefore we show in Fig. 2(b) the predicted pump depletion η_p in terms of $\Lambda_{R,p}$ and ρ, for a suitably apodized nominally linearly chirped QPM grating, modelling a spectral component phase-matched in the middle of the grating. Example curves showing propagation of the seeded signal wave versus position in the grating are also shown in Fig. 2(a) for several values of ρ at constant $\Lambda_{R,p} = 2$ to illustrate the process being modelled.

Figure 2 can provide guidelines for the values of ρ required in a final power amplifier stage in order to effectively saturate the pump. For example, obtaining a peak conversion efficiency of 80% at a reasonable small-signal gain parameter of $\Lambda_{R,p} \approx 2$ [corresponding to $G_s = \exp(2\pi\Lambda_{R,p}) \approx 2.9 \times 10^5$] requires a corresponding value of $\rho = 10^{-2}$, which then places constraints on pre-amplifier stages to achieve such an input photon flux. If the input photon flux is limited to $\rho = 10^{-3}$ by the pre-amplifier properties, 80% peak conversion efficiency requires $\Lambda_{R,p} = 3$, which may be challenging in practice (for example due to the effects discussed in section 5), and will also lead to additional noise amplification. Achieving such a high peak

#205795 - $15.00 USD Received 4 Feb 2014; revised 3 Apr 2014; accepted 8 Apr 2014; published 15 Apr 2014

conversion efficiency (i.e. corresponding to the peak of the pump intensity profile in space and time) is important, since the total efficiency will be lower (unless using shaped, e.g. flat-top beam and pulse profiles). Based on these considerations, combined with estimations of overall system performance via simulations based on Eq. (1), as well as the effects considered in later sections of this paper, we split our OPCPA system into three OPA stages, as depicted in Fig. 1. The stages have low pump depletion in OPA1, moderate depletion in OPA2, and substantial depletion in OPA3. We summarize the various system design considerations in subsection 8.1.

Concerning the applicability of Fig. 2, the use of chirped pulses helps to support the assumption of a series of continuous wave interactions [see Eq. (10) for example; we revisit this point in more detail in section 7]. With the use of sufficiently wide beams (while maintaining the required intensities), diffraction can be neglected [see also section 4]. However, even under these conditions, the interaction is still complicated by the temporally and transverse-spatially varying intensities of the pump and signal beams. To obtain quantitative predictions of total system conversion efficiency, numerical simulations [see Eq. (1)] are required. Our focus in this paper is on establishing the relevant physics and constraints, which can then guide more detailed numerical simulations or adjustments of experimental conditions, with which performance can be optimized around a nominal system layout.

4. Transverse beam effects: suppression of gain guided modes

The plane-wave physics discussed in section 3 can break down due to non-collinear gain-guiding effects. Gain guiding is a general feature of OPA, but has unique properties for the case of chirped QPM gratings, due to the combination of transverse spatial walk-off of the signal and idler waves and dephasing due to the QPM chirp [3]. Under certain conditions [3, 52], non-collinear gain-guided modes can exist where the signal and idler fields adapt during amplification to the QPM grating chirp, enabling amplification over long distances. As a result, the overall gain of such modes can greatly exceed that of the desired collinear OPA interaction. If the modes are seeded by quantum noise, this process results in a large increase in the optical parametric generation (OPG) background of the system. If the modes are seeded by the desired signal or idler wave, the result can be a reduction in beam quality. While the noise content at the output of the device can be partly reduced by spatial filtering, eventually the noise can be amplified to the point where it saturates the pump. It is thus critical in designing an OPCPA system to ensure that these gain-guided modes are suppressed. The essential physics of these gain-guided modes was considered in [3, 52], and can be modelled using Eq. (1) assuming idler, signal and pump waves, and neglecting dispersion. Here, we consider the case of broadband OPCPA: we show that with proper system design, gain guided modes can be fully suppressed, enabling high-noise-contrast amplification [1].

4.1. Non-collinear phase-matching conditions

We first introduce non-collinear phase-matching in the context of QPM devices. We assume a plane-wave interaction with k-vectors $\mathbf{k}_j$ for $j \in \{i,s,p\}$ and a grating k-vector $\mathbf{K}_g$. Each $\mathbf{k}_j$ satisfies $|\mathbf{k}_j| = k(\omega_j)$, where $k(\omega_j)$ is one of the propagation constants associated with the direction of $\mathbf{k}_j$. The vector phase mismatch is given by

$$\boldsymbol{\Delta k} = \mathbf{k}_p - \mathbf{k}_s - \mathbf{k}_i - \mathbf{K}_g \tag{17}$$

This equation can support phase-matching ($\boldsymbol{\Delta k} = \mathbf{0}$) for both collinear and non-collinear signal and idler waves. We assume $\mathbf{k}_p = k_p \hat{\mathbf{z}}$ and $\mathbf{K}_g = K_g \hat{\mathbf{z}}$ for scalars $k_p = k_e(\omega_p)$ and K_g. Phase-matching along the transverse coordinates x and y implies that the transverse components of $\mathbf{k}_i$ and $\mathbf{k}_s$ are equal and opposite. The z-component of the resulting phase mismatch can be written as a function of the transverse spatial frequency components of the signal. As before,

#205795 - $15.00 USD Received 4 Feb 2014; revised 3 Apr 2014; accepted 8 Apr 2014; published 15 Apr 2014

we assume a uniaxial crystal, extraordinary-polarized waves, and small propagation angles with respect to the c-axis, resulting in

$$\frac{\mathbf{k}_j \cdot \hat{\mathbf{z}}}{k_e} \approx 1 - \frac{1}{2}\left[\left(\frac{\mathbf{k}_j \cdot \hat{\mathbf{x}}}{k_o}\right)^2 + \left(\frac{\mathbf{k}_j \cdot \hat{\mathbf{y}}}{k_e}\right)^2\right]. \tag{18}$$

Since the magnitudes of the transverse spatial frequencies for the signal and idler are equal, it is useful to define $k_x = \mathbf{k}_s \cdot \hat{\mathbf{x}}$ and $k_y = \mathbf{k}_s \cdot \hat{\mathbf{y}}$. By applying these definitions and substituting Eq. (17), the z component of the phase mismatch can be written as

$$\mathbf{\Delta k} \cdot \hat{\mathbf{z}} \approx \Delta\beta + \sum_{j=i,s}\left[\frac{k_e(\omega_j)}{2k_o(\omega_j)^2}k_x^2 + \frac{1}{2k_e(\omega_j)}k_y^2\right] \tag{19}$$

where $\Delta\beta = k_e(\omega_p) - k_e(\omega_s) - k_e(\omega_i) - K_g$ is the collinear phase mismatch introduced in Eqs. (8a) and (8b). With some additional assumptions, Eq. (19) can be simplified significantly. If we neglect the anisotropy of the material (via the substitution $k_o \to k_e$), define the resulting magnitude of the transverse components of the k-vectors as $k_\perp = (k_x^2 + k_y^2)^{1/2}$, simplify the resulting coefficients of $k_\perp$ with the approximation $k_i + k_s \approx k_p$, and define a geometric mean angle according to

$$\theta_{is} = \pm\frac{|k_\perp|}{\sqrt{k_e(\omega_i)k_e(\omega_s)}}, \tag{20}$$

then Eq. (19) can be simplified as

$$\mathbf{\Delta k} \cdot \hat{\mathbf{z}} \approx \Delta\beta + \frac{k_e(\omega_p)}{2}\theta_{is}^2. \tag{21}$$

From Eqs. (19) and (21), $\mathbf{\Delta k} \cdot \hat{\mathbf{z}} > \Delta\beta$. Hence, non-collinear phase-matching can be obtained whenever $\Delta\beta < 0$ (within the limits of the small-angle approximation). Note that the phase-matching angle $\theta_{is}(z,\Omega)$ is frequency-dependent, mainly due to the frequency dependence of $\Delta\beta(z,\Omega)$. Frequency dependencies have been suppressed in the above equations for compactness. Note also that in a chirped QPM grating, $\Delta\beta(z,\Omega)$, and hence the phase-matching angle $\theta_{is}(z,\Omega)$, changes with position, and hence the required mean angle of the signal and idler fields must be able to evolve with position as well for amplification to continue; it turns out that this evolution is connected with the size of the pump beam.

4.2. Non-collinear gain-guiding cut-offs

The gain-guided modes supported in chirped QPM devices were considered experimentally and theoretically in [3], and then in additional theoretical detail in [52]. The main processes which determine the gain rate are: the rate of spatial walk-off, determined by the size of the pump beam and by the phase-matched signal and idler angles; the rate of dephasing, determined by the QPM chirp rate; and the coupling rate between the signal and idler fields, given by γ_p. We can thus define a gain distance $L_g = \gamma_p^{-1}$, a walk-off distance $L_{wo} = w_p/\theta_{is}$, and a dephasing distance $L_{\text{deph}} = 2\gamma_p/|\Delta k'|$ [see also Eq. (14)]. This dephasing distance can be understood in the context of Eq. (10): it is the distance required for the integrand to go from its peak, with $(\Delta k_0 - K_g) = 0$, to zero, with $(\Delta k_0 - K_g) = 2\gamma_p$ (for a plane-wave interaction).

The exponential gain rate Γ of the gain-guided modes can be normalized to the maximum possible gain rate γ_p associated with collinear, plane-wave propagation. Figure 3(a), adapted from [3], shows this normalized gain rate (for the electric field) as a function of $L_g/L_{wo} = \theta_{is}/(\gamma_p w_p)$ for several values of $L_{\text{deph}}/L_g = 2\gamma_p^2/|\Delta k'| = 2\Lambda_{R,p}$. The quantity L_g/L_{wo} can be

#205795 - $15.00 USD Received 4 Feb 2014; revised 3 Apr 2014; accepted 8 Apr 2014; published 15 Apr 2014

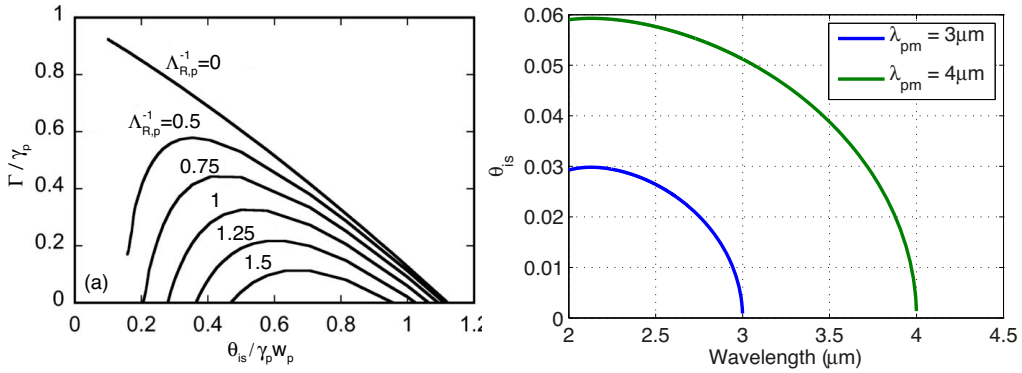

Fig. 3. (a) Simulated normalized gain rate Γ/γ_{p0} of non-collinear gain guided modes, for different normalized angles and values of $\Lambda_{R,p}$. The $\Lambda_{R,p}^{-1}=0$ case corresponds to an unchirped grating. This figure is adapted from Fig. 2 of [3] and Fig. 12 of [52], with minor modifications to notation. (b) Geometric mean angle θ_{is} versus idler wavelength, for two particular grating k-vectors (chosen to satisfy collinear phase-matching for 3 or 4 μm). The maximum angle occurs at degeneracy.

viewed as a normalized angle, $\bar{\theta}=\theta_{is}/(w_p\gamma_p)$, while $\Lambda_{R,p}$ determines the overall small-signal plane-wave gain, as discussed in section 3.

For sufficiently large phase-matching angles, gain guiding is suppressed because the signal and idler beams walk off the pump faster than they are amplified; for sufficiently small angles, gain guiding is suppressed in the case of chirped QPM gratings because the beams are dephased faster than they walk off the pump [3]. It is this latter property that allows the modes to be suppressed in practice. From Fig. 3, an approximate condition for the gain to be cut-off is

$$\frac{\theta_{is}}{\gamma_p w_p} \lesssim \frac{1}{\pi\Lambda_{R,p}}. \tag{22}$$

This condition can be expressed as $L_{\text{deph}}/L_{wo}<(2/\pi)$, i.e. that the waves dephase before they walk off the pump.

Fig. 3(a) and Eq. (22) show that sufficiently small normalized phase-matching angles are required in order to suppress gain guided modes. Therefore, to see how to obtain this condition in practice, we next determine the range of phase-matching angles supported by the crystal, for a given QPM grating profile. The range of $K_g(z)$ associated with the nominal part of the grating (i.e. excluding apodization regions) is determined primarily by the required spectral bandwidth, although it depends on γ_p as well [see Eq. (15)]. For a given material and pump wavelength, there is a range of the material phase mismatch $\Delta k_0(\Omega)$ [see Eq. (12)]. For each frequency shift Ω, the largest phase-matching angle is the one corresponding to the most-negative value of $\Delta\beta(z,\Omega)$, and hence to the largest grating k-vector contained in the nominal grating profile, which we denote $K_{g,\max}$; if for a particular frequency $\Delta\beta(z,\Omega)>0$, then no gain-guided modes are supported for that frequency. We therefore arrive at the largest phase-matching angle associated with each frequency shift Ω from some chosen carrier frequency:

$$\theta_{is,\max}(\Omega)\approx \text{Re}\sqrt{\frac{2(K_{g,\max}-\Delta k_0(\Omega))}{k_p}}, \tag{23}$$

Fig. 3(b) shows the geometric mean angle θ_{is} as a function of idler wavelength, assuming a 1064-nm pump and an MgO:LiNbO$_3$ QPM grating, for two grating k-vectors, chosen to

#205795 - $15.00 USD Received 4 Feb 2014; revised 3 Apr 2014; accepted 8 Apr 2014; published 15 Apr 2014

satisfy collinear phase-matching of 3 or 4 μm [53]. In a grating supporting amplification across this spectral range, the curve corresponding to 4 μm would closely represent $\theta_{is,\max}$, up to a correction to the range of grating k-vectors needed based on Δk_{OPA} given in Eq. (15). It is useful to note that for the chosen configuration, $\theta_{is,\max}$ corresponds to degeneracy ($\lambda_i = \lambda_s = 2\lambda_p$).

Quantum noise seeds the amplifier at all temporal and spatial frequencies, and we thus require that Eq. (22) be satisfied for *all* frequencies Ω, not just those we are trying to amplify, in order to fully suppress gain-guided modes. For a collinear interaction, a given material, and a given pump wavelength, $\theta_{is,\max}(\Omega)$ is essentially fixed by the required gain bandwidth (since this determines the range of grating k-vectors required). For the purposes of OPCPA system design, the remaining degree of freedom to satisfy Eq. (22) is the factor $\gamma_p w_p$, which must be sufficiently large. Since γ_p^2 is proportional to pump intensity, $(\gamma_p w_p)^2$ is proportional to the peak power of the pump, independent of its beam size. Thus, suppression of gain guided modes requires using a pump of sufficient peak power. To quantify this constraint, we substitute Eq. (23) into Eq. (22) and express $\gamma_p w_p$ in terms of the pump peak power, which yields

$$P_{pk} > \frac{\pi^3 \varepsilon_0 n_i n_s n_p c^3}{4\omega_i \omega_s d_{33}^2 d_1^2} \left(\Lambda_{R,p} \theta_{is,\max}\right)^2, \tag{24}$$

where the signal and idler quantities in this equation should be evaluated at the frequencies corresponding to $\theta_{is,\max}$. We have written Eq. (24) in terms of $\Lambda_{R,p}$ since this gain factor is fixed by the desired OPCPA gain.

4.3. Implications for OPCPA

Consider an example with a 1.064-μm pump pulse and a 50%-duty-cycle QPM grating in an MgO:$LiNbO_3$ crystal. The relevant nonlinear coefficient for OPA is $d_{33} \approx 19.5$ pm/V [54]. For a range of K_g satisfying phase-matching between 3- and 4-μm, $\max(K_g) \approx 2.198 \times 10^5$ m^{-1}, which results in a maximum angle $\theta_{is,\max} \approx 0.06$. This angle occurs at pump degeneracy, so the corresponding signal and idler frequencies are $\omega_i = \omega_s = \omega_p/2$. For these parameters, Eq. (24) can be expressed as

$$P_{pk} > (0.56\,\mathrm{MW}) \times \Lambda_{R,p}^2. \tag{25}$$

For peak powers below this level, there will exist a finite range of signal frequencies which can excite gain-guided modes, and thereby experience excessive gain through non-collinear phase-matching. Note that Eq. (25) should be satisfied both for pre-amplifier as well as power-amplifier stage(s).

For Gaussian pump pulses with 12-ps FWHM duration and an energy of 400 μJ, the peak power is 31.3 MW. If 10% of the pulse is used for a pre-amplifier stage, Eq. (25) can be satisfied, within a good margin, while still obtaining high gain (e.g. $\Lambda_{R,p} > 2$). In contrast, with a 100-μJ pump such as the one used in our earlier OPCPA experiments [4] (prior to the implementation of an additional amplifier [44]), satisfying Eq. (25) in a high-gain pre-amplifier stage is quite challenging. In our current OPCPA system shown in Fig. 1, the average powers reaching OPA1, OPA2, and OPA3 are 5.7 W, 3.8 W, and 15.2 W, respectively. The peak power inside the (uncoated) crystals is relevant for considering gain-guided mode properties; these internal peak powers are approximately 7.7 MW, 5.1 MW, and 20.6 MW, respectively. Operation at 50 kHz and re-using the transmitted pump from OPA1 to pump OPA2 ensured that we are able to satisfy Eq. (25) in each OPA stage, even for relatively large values of $\Lambda_{R,p} \sim 3$. Experimentally, we observe no evidence of gain-guided mode related effects, and demonstrate good OPG properties of the overall system (as discussed in more detail in [1]), indicating that we have indeed suppressed these modes.

#205795 - $15.00 USD Received 4 Feb 2014; revised 3 Apr 2014; accepted 8 Apr 2014; published 15 Apr 2014

5. Role of QPM duty cycle errors

In the previous section, we considered an unwanted effect which can arise due to the use of finite-sized beams. In the following sections, we consider plane-wave interactions, but go beyond the three-wave mixing processes modelled by Eqs. (8a) and (8b). We first consider the effects on OPCPA of random duty cycle (RDC) errors in the QPM grating. We recently studied such effects in detail for several device configurations [50], including parasitic pump SHG in the context of OPCPA. Here, we review the relevant results of [50], and then expand on the analysis for the specific case of OPCPA. Note that while our focus in this paper is on the case of chirped QPM gratings, RDC errors are relevant for OPCPA employing both chirped and unchirped gratings, and explain the intense green light typically generated in 1-μm-pumped QPM-based OPCPA systems; our results in this section are applicable to both chirped and unchirped gratings.

5.1. Essential features of QPM gratings with RDC errors

A schematic of RDC errors is depicted in Fig. 4(a). For these types of errors, the statistics of the QPM domain boundaries (from sample to sample) are assumed to be independent, identical, normal distributions. The mean boundary positions (corresponding to the nominal grating design) are denoted $\mathbf{z}_0[n]$ for boundary n (element n of vector $\mathbf{z}_0$), and their standard deviations are σ_z. As an example of this notation, for a periodic 50-% duty cycle grating with period $2l_D$ and domain length l_D, $\mathbf{z}_0[n] = nl_D$. RDC errors lead to a pedestal in the spatial frequency spectrum of the grating which is approximately flat after performing an ensemble-average over many gratings with different random errors.

To quantify the pedestal, we state the ensemble average of the spatial frequency spectrum of the QPM grating, denoted $\left\langle |\tilde{g}_{\mathbf{z}}(k)|^2 \right\rangle$ for longitudinal spatial frequency k. From Eq. (9) of [50], this averaged spectrum is given by

$$\left\langle |\tilde{g}_{\mathbf{z}}(k)|^2 \right\rangle = e^{-k^2\sigma_z^2} |\tilde{g}_{\mathbf{z}_0}(k)|^2 + N \left(\frac{\pi}{kL}\right)^2 \left(1 - e^{-k^2\sigma_z^2}\right), \tag{26}$$

where $\mathbf{z}_0$ is the vector of ideal (designed) grating domain boundary positions, $\mathbf{z}$ is a vector of actual boundary positions (including RDC errors), and N is the number of domains in the grating. For a given grating, $|\tilde{g}_{\mathbf{z}}(\Delta k)|^2$ is proportional to the cw conversion efficiency for spectral components having material phase mismatch Δk. For a periodic grating of period $2l_D$, $|\tilde{g}_{\mathbf{z}_0}(\Delta k)|^2$ is thus approximately a sinc^2 function in the vicinity of first-order QPM ($\Delta k \approx \pi/l_D$), and is normalized to have peak equal to 1; see Eq. (10) of [50]. The second term in Eq. (26) is a noise pedestal that originates from the RDC errors; it applies for gratings with at least several domains ($N \gg 1$). It leads to an enhancement of the conversion efficiency for nominally phase-mismatched processes.

Fourier spectra of an example apodized chirped MgO:LiNbO$_3$ grating, designed for mid-IR OPCPA, are illustrated in Fig. 4(b). We assume RDC errors with $\sigma_z = 0.5$ μm. The figure shows ideal, actual, and ensemble-averaged spectra. For the ensemble average, averaging is performed over 250 gratings with different errors. The regions corresponding to some additional processes are also shown by vertical dashed lines (idler-pump SFG; signal-pump SFG; and pump SHG). In particular, pump SHG is relatively close to 5$^{\text{th}}$-order QPM. The efficiency of these nominally phase mismatched processes are enhanced by RDC errors, and also, potentially, by the apodization profile employed (since it broadens the wings of the phase-matching regions).

RDC errors can also influence the desired process directly. This is illustrated by Fig. 4(c), which shows the same curves as Fig. 4(b) but plotted on a linear scale in the vicinity of first-order QPM. There is a residual fluctuation in the ideal (blue) curve due to imperfect apodization. The averaged (black) curve closely corresponds to the ideal grating, apart from a $\exp(-k^2\sigma_z^2)$

#205795 - $15.00 USD Received 4 Feb 2014; revised 3 Apr 2014; accepted 8 Apr 2014; published 15 Apr 2014

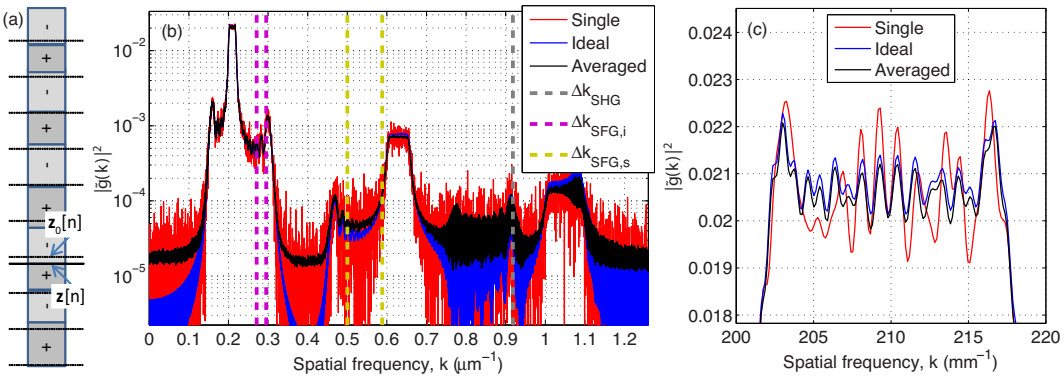

Fig. 4. (a) Schematic of a QPM grating with random duty cycle (RDC) errors. Horizontal dashed lines indicate the ideal, equally-spaced domain boundary positions. Elements of the domain boundary vectors $\mathbf{z}$ (with RDC errors) and $\mathbf{z}_0$ (ideal) are indicated. (b) Fourier spectra $|\tilde{g}(k)|^2$ with parameters $\sigma_z = 0.5$ μm and a 10-mm crystal, and approximately a 30 μm average period. For the averaged case (black curve), averaging is performed over 250 gratings. The vertical dashed lines show the spatial frequencies corresponding to phase-matching for some additional processes (signal-pump SFG; idler-pump SFG; and pump SHG). (c) The same curves as (b), but shown on a linear scale in the vicinity of first-order QPM. This plot reveals the influence of RDC errors on the nominal 'tuning curve' of the device.

scale factor which originates from the first term in Eq. (26). The single (red) curve shows an individual grating with RDC errors, and clearly exhibits additional fluctuations compared to the other curves. This effect will apply to all chirped QPM devices (not just OPCPA devices), causing distortions to their "tuning curves", and should therefore not be ignored; it emphasizes the importance of minimizing RDC errors through fabrication improvements in the future.

5.2. *Implications for QPM-based OPCPA*

The RDC-enhanced efficiency of processes such as pump SHG can be calculated via $\tilde{g}(k)$. When using narrow-band pulses, this efficiency can fluctuate versus crystal temperature (as in any phase-matching process) and due to lateral translation of the nonlinear crystal (if the RDC errors vary along this coordinate). When using ultrashort pulses, however, the efficiency can correspond closely to the ensemble average in Eq. (26), if the bandwidth of the pulses exceeds the "natural linewidth" of the QPM peak (that is, the bandwidth for an ideal periodic grating). Following the approach of Eq. (19) of [50], the pump SHG conversion efficiency can be estimated. It is convenient to express the result in terms of the characteristic quantities associated with the OPA process. Assuming Gaussian beam profiles and a sech^2 pump temporal profile, we find

$$\frac{\langle U_{SH}\rangle}{U_p} \approx \frac{1}{3}\left(\frac{1-e^{-\Delta k_{SHG}^2\sigma_z^2}}{\Delta k_{SHG}^2\sigma_z^2}\right)\left(\frac{\pi\sigma_z}{l_D}\right)^2\left(\frac{n_i n_s}{n_{SH}n_p}\frac{\omega_p^2}{\omega_i\omega_s}\frac{d_{SHG}^2}{d_{OPA}^2}\right)\left(\gamma_p^2 L l_D\right). \tag{27}$$

Note that for a Gaussian temporal profile, the $1/3$ factor becomes $1/(2\sqrt{2})$. In Eq. (27), the first quantity in parenthesis approaches 1 for small RDC errors, and the third quantity in parentheses corresponds to the different strengths of the SHG and OPA interactions. In terms of chirped QPM OPA quantities, $\gamma_p^2 L = \Lambda_{R,p}\Delta k_{BW}$, and hence this product is determined mainly by the required gain and spectral bandwidth. As such, assuming the RDC-related contributions to SHG

#205795 - $15.00 USD Received 4 Feb 2014; revised 3 Apr 2014; accepted 8 Apr 2014; published 15 Apr 2014

dominate, the ensemble-averaged SHG efficiency is a function only of the OPA requirements and the RDC errors. For unchirped devices, $\gamma_p^2 L$ is also proportional to the product of the k-space gain bandwidth of the device times the logarithmic gain [2], which are also constrained quantities.

In our OPCPA system [1], we observe the pump SHG to vary ($\sim$factor-of-2 changes) due to lateral translation of the crystal even in OPA1 and OPA2, in which the grating is 3-mm-wide and the beams are only a few hundred μm wide, suggesting some inhomogeneity in the QPM duty cycle errors along the grating width. We also observe the pump SHG to fluctuate with temperature, exhibiting a dependence consistent with RDC errors (again, $\sim$factor-of-2 changes over a range of $\approx 100\ ^\circ$C), given the acceptance bandwidth of the device with respect to pump- and second-harmonic frequencies. Experimentally, in OPA1 and OPA2 we translate the QPM gratings laterally and optimize their temperature to minimize pump SHG. In OPA3, the beam width is comparable to the grating width, so we only optimize with respect to temperature.

As discussed in [50], at the corresponding intensities of green light, two-photon absorption (TPA) can become significant, which may lead to photorefractive effects or an excessive thermal load on the crystal; it is also worth noting that such TPA-induced photorefraction may differ phenomonologically from normal one-photon photorefraction. After an analysis similar to that detailed in [50], the TPA can be estimated as

$$\frac{\langle U_{TPA}\rangle}{U_p} \approx \frac{24}{35}\left(\frac{\langle U_{SH}\rangle}{U_p}\right)^2 \left(\beta_{TPA} I_{p,pk} L\right) \tag{28}$$

where β_{TPA} is the two-photon absorption coefficient for the SH. Note that the $24/35$ factor becomes $2/3$ for a Gaussian pulse. The TPA is clearly related to the SHG efficiency given by Eq. (27), but also includes the final factor in parenthesis, which is the TPA factor for a SH pulse having intensity equal to the peak of the pump, neglecting TPA-induced changes to that intensity; this factor can be quite large. Note also that we have assumed small losses, which is a reasonable constraint to apply to a practical system.

To quantify the powers expected for SHG and TPA, we next apply Eqs. (27) and (28) to our OPCPA system, assuming $\sigma_z = 0.5$ μm, a nonlinear coefficient of 19.5 pm/V for the OPA process and 25.2 pm/V for the pump-SHG process. Based on our measured powers and beam sizes, we estimate peak pump intensities inside the OPA1, OPA2, and OPA3 stages of 4.9, 6.8, and 4.4 GW/cm^2, respectively. For these values, we predict generated SHG powers (directly after the uncoated crystals) of 188, 171, and 446 mW; note that with a slightly different $\sigma_z = 0.4$ μm, the latter value would be 296 mW. These predictions are in good agreement with the $\approx$ 300 mW green power we observe after OPA3 at full power. Using the same parameters and the TPA coefficient of $LiNbO_3$ [55], Eq. (28) predicts two-photon-absorbed powers of 13.6, 23.1, and 25.6 mW, respectively.

At intensities somewhat above those reported in [1], we begin to observe slight time-dependent fluctuations in the generated green light, and also fanning of the transmitted pump beam along the crystal c-axis. These observations appear consistent with photorefractive effects arising from the non-negligible TPA predicted by Eq. (28). Several photorefractive effects relevant to our operating regime have been studied, for example, in Refs. [56–58]. While the photorefractive effects we observe seem to be completely reversible, they place a limit on the signal-idler coupling rate γ_p which we can employ, and hence on the single-pass small-signal gain, and other properties of the amplifiers. A more detailed theoretical and experimental study of such photorefractive effects in the high-power, high-intensity, QPM, TPA-dominated absorption regime may be warranted, to elucidate the most important material properties, beyond the RDC characteristics, for maximizing the signal-idler coupling rate in the context of OPCPA.

#205795 - $15.00 USD Received 4 Feb 2014; revised 3 Apr 2014; accepted 8 Apr 2014; published 15 Apr 2014

6. Spectral effects: coincidentally phase-matched processes

Even in an ideal structure without any RDC errors, a number of factors can cause the minimal plane-coupled-wave model considered in subsections 3.2 and 3.3 to break down. For example, many components of the nonlinear polarization are neglected by the three-wave mixing equations (8). In deriving these equations, the only components of the nonlinear polarization that were retained were those with carrier frequency equal to that of the idler, signal, or pump. In this section, we consider several additional processes, explaining their influence on QPM OPCPA, in particular when using chirped gratings. Our main focus will be on $\chi^{(2)}$ sum and difference frequency mixing processes. We justify this focus in appendix A, where we estimate the severity of several $\chi^{(3)}$ and $\chi^{(3)}$-like processes.

6.1. Phase-matching of additional $\chi^{(2)}$ mixing processes

We can gain information about the significance of the neglected $\chi^{(2)}$ terms for a chirped-QPM OPCPA device by performing a series of phase-matching calculations, assuming a pump with a single-frequency component ω_p. For each signal frequency ω_s, all sum and difference frequencies involving ω_s, ω_p, and $\omega_i = \omega_p - \omega_s$ are generated (and in turn, all processes involving sums and differences of the resulting set also occur, and so on). As an example, the most relevant DFG-like process (excluding the OPA process itself) is the generation of frequency $\omega_{DF} = |\omega_s - \omega_i|$; the corresponding phase mismatch for this process is

$$\Delta k_{si}^{(DFG)} = k_e(\omega_s) - k_e(\omega_s - \omega_i) - k_e(\omega_i), \tag{29}$$

where this equation assumes $\omega_s > \omega_i$. Many SFG processes also occur, generating frequencies $\omega_{pq}^{(SFG)} = \omega_p + \omega_q$ for indices p and $q \in \{i, s, p\}$. The corresponding phase mismatches are given by Eq. (6).

The phase mismatches can be compared to the range of grating k-vectors required to quasi-phase-match the desired OPA process (which would be $\Delta k_{is}^{(SFG)}$ in the above notation) by plotting each $\Delta k_{pq}(\omega_s)$ over the frequency range of interest. In Fig. 5, we plot the phase-matching period Λ for several processes, assuming a pump wavelength of 1.064-μm and all-e-wave polarized interactions in a MgO:$LiNbO_3$ crystal operated at 150°C. For the purposes of the figure we assume $\omega_s > \omega_i$ (that is, signal refers to the short-wavelength wave).

To interpret Fig. 5, consider an example case where OPA phase-matching must be satisfied for idler wavelengths between 3-4 μm: the corresponding range of grating periods is approximately 28.6-30.9 μm (solid blue curve). Consider the 3.8-μm idler component. If the grating is positively chirped ($\Delta k' > 0$; short QPM periods near the input end of the crystal) then this component is first amplified where the local period is ≈ 29.1 μm. Near the end of the grating, where the period is ≈ 30.5 μm, SHG of this component is satisfied. If the amplified idler is sufficiently intense, this process can be efficient, leading to distortions of the pulse and a reduction in efficiency. If an even wider range of periods is present, for example 28-32 μm, then the idler is first amplified where the period $\Lambda \approx 29.1$ μm, up-converted to its SH around $\Lambda \approx 30.5$ μm, and this SH is itself amplified (by the pump of frequency ω_p) around $\Lambda \approx 31.7$ μm (dashed curve). If the SHG process is reasonably efficient, then the idler SHG can effectively experience OPA twice, and hence have very high gain. Similar arguments can be made for the other spectral components and processes illustrated. When the QPM periods for different processes are quite close, the k-space extent of these processes is important (for example, OPA occurs over the region for which $|\Delta k| < 2\gamma_p$).

In apodizing the grating, a highly nonlinear chirp profile is imposed at the beginning and end of the device to achieve a weak interaction at the input and output regions [8]. Such a profile entails a wide range of QPM periods, and hence the period is swept through the various processes

#205795 - $15.00 USD Received 4 Feb 2014; revised 3 Apr 2014; accepted 8 Apr 2014; published 15 Apr 2014

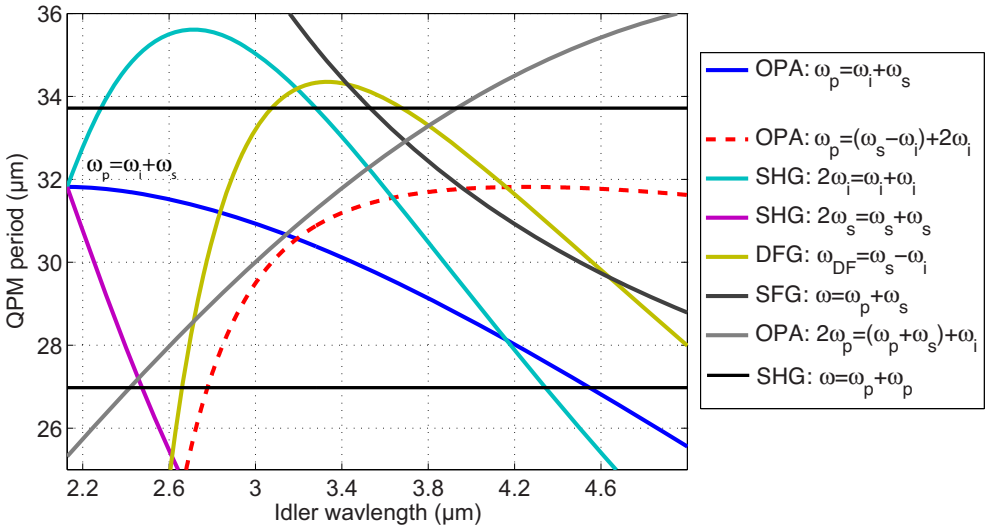

Fig. 5. Coincidentally phase-matched processes, assuming a pump wavelength of 1.064 μm, as a function of the long-wave idler wavelength. The legend indicates the type of interaction (SHG, OPA, or SFG) and the frequencies involved. The desired OPA interaction is $\omega_p = \omega_i + \omega_s$; the corresponding curve is indicated. For each process, we consider phase-matching for the nearest-odd-order of QPM (except for pump SHG process, for which we show 4^{th}- and 5^{th}-order QPM).

illustrated in 5. For example, the period may be swept through pump SHG phase-matching. Even though the chirp rate is rapid, the pump may be intense enough for the SHG process to have non-negligible efficiency. Since pump SHG occurs at 4^{th}- and 5^{th}-order QPM, it is possible in principle to suppress this process by an appropriate choice of QPM duty cycle in the regions where SHG phase-matching is satisfied (50% for 4^{th}-order, and 40% or 60% for 5^{th}). This level of control of the duty cycle can be challenging in practice. Therefore, it is important to maximize the chirp rate in the apodization regions (while still keeping the apodization itself effective) so as to minimize the efficiency of such processes; we discussed such optimal procedures for apodization in [8].

Based on Fig. 5, in order to avoid efficient long-wave SHG ($2\omega_i = \omega_i + \omega_i$) in a collinear amplifier designed for wavelengths between 3 and 4 μm, the chirp rate should be negative ($\Delta k' < 0$), since with this choice SHG of the long-wave idler is phase-matched before that idler has been amplified via the OPA process, and so the parasitic SHG process has low efficiency. It is for this reason that we use a negative chirp rate in all of our OPCPA stages.

6.2. Numerical Example

When the phase-matching regions for the different processes are sufficiently separated, simple expressions for their efficiency can be obtained. This is not always the case, however, so it is useful to simulate all of the processes which are close to or pass through phase-matching using the generalized coupled-envelope model in Eq. (1).

In the examples shown in Fig. 6(a) and 6(b), we consider quasi-cw interactions involving several different spectral components. The set of frequencies included in these simulations is as follows: ω_i, ω_s, ω_p, $2\omega_i$, $2\omega_s$, $2\omega_p$, $(\omega_i + \omega_p)$, $(\omega_s + \omega_p)$, and $(\omega_s - \omega_i)$. The assumed parameters are $\Lambda_{R,p} = 2$ and $\rho = 10^{-6}$. The chirp rate $|\Delta k'| = 3$ mm^{-2}, and grating length $L = 10$ mm.

#205795 - $15.00 USD Received 4 Feb 2014; revised 3 Apr 2014; accepted 8 Apr 2014; published 15 Apr 2014

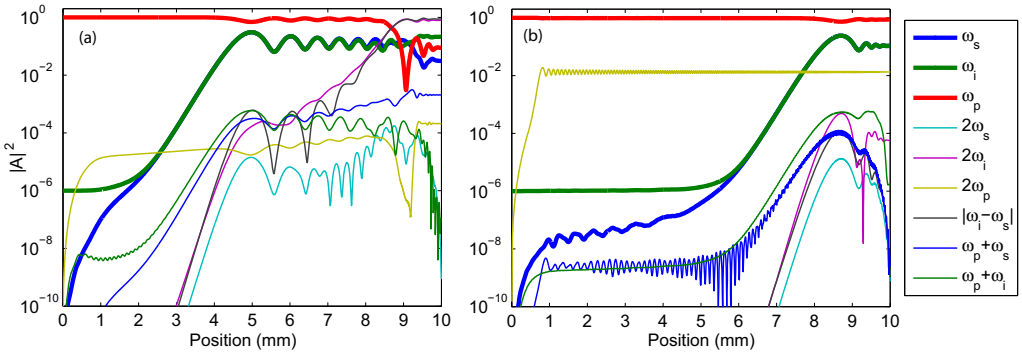

Fig. 6. Numerical example including several carrier waves. The pump and seeded idler wavelengths are 1.064-μm and 3.8-μm, respectively. The legend shows the frequency of each wave included in the model. The sign of the chirp rate (sgn($\Delta k'$)) is (a) positive (showing significant coupling to unwanted field envelopes and hence distortion of the desired OPA process), and (b) negative (showing negligible distortions). The parameters are given in the text

Several features are apparent from these figures. In Fig. 6(a), where the chirp rate is positive, the signal and idler are fully amplified around 5 mm from the input. Shortly after this point, the idler SHG process is phase-matched, and then the idler-SH OPA process is phase-matched. This latter process leads to exponential growth of the $(\omega_s - \omega_i)$ and $(2\omega_i)$ spectral components. Near the end of the grating, these components actually become stronger than the idler and signal themselves, and can even deplete the pump. This operating regime is poorly suited to OPCPA. The other curves in Fig. 6(a) exhibit no prominent features, except an overall growth for up-converted components, since these are driven by waves which are amplified.

The behavior of Fig. 6(b), where the chirp rate is negative, is much more favorable. The only non-negligible waves at the output are the desired signal and idler, the pump, and a significant but still comparatively small pump second harmonic (which may actually be further enhanced in reality due to the RDC errors in the grating, as discussed in section 5). Since idler SHG and idler-SH-OPA occur earlier in the grating than idler OPA, these former two processes are inefficient and do not play a significant role. Therefore, the undesired coincidentally-phase-matched processes which occur in 6(a) have been avoided by using a negative chirp rate.

7. Temporal dynamics: saturation and group velocity mismatch

The quasi-cw chirped-pulse limit we have assumed so far breaks down when the relative group delay between the idler, signal and pump accumulated during propagation through the QPM grating is too large with respect to their (stretched) durations. While the fact that such breakdown occurs is obvious, the point at which it does, and the implications of the breakdown mechanism(s) for system design, are not always obvious.

In this section, we show how this breakdown can in some situations lead to pronounced ripples in the output signal spectrum, even in apodized QPM gratings. We explain the physics of these ripples, and how they can be suppressed by appropriate combinations of pulse and grating chirp rates (i.e. by overall design of the OPCPA system), while still satisfying other constraints of the system and QPM devices (such as the requirement of $\Delta k' < 0$ imposed by the coincidental phase-matching issues discussed in section 6).

#205795 - $15.00 USD Received 4 Feb 2014; revised 3 Apr 2014; accepted 8 Apr 2014; published 15 Apr 2014

7.1. *Effects of group velocity mismatch (GVM)*

To explain the important effects involved in saturated chirped QPM OPA devices in combination with non-zero temporal walk-off between the interacting signal, idler, and pump waves, we first consider the much simpler case of unsaturated amplification of an unchirped signal input (seed) pulse. Given imperfect apodization, two idler pulse components are generated at the input to the device.

The temporal structure of the pulses in chirped QPM OPA with an unsaturated, continuous-wave pump was discussed in [59]. The evolution of the waves in the saturated-pump regime, and the influence of QPM apodization, was discussed in detail in [8]. More specifically, the existence of two idler pulse components is evident from several other sources. For example, in Eq. (E5) of [2], which represents the signal and idler in the frequency domain for an undepleted-pump chirped-QPM OPA device, multiple idler pulse components are implied by setting $A_{s0} = 0$ and then interchanging the *i* and *s* subscripts. That equation is still quite accurate near the *input* of saturated OPA devices, provided the signal and idler are much weaker than the pump. The two pulse components can also be understood in the context of cascaded $\chi^{(2)}$ interactions, the physics of which are relevant to chirped QPM devices in spatial regions where the phase-mismatch is high for all of the spectral components involved. As an example, see the two second-harmonic pulse components illustrated in Fig. 5(b) of Ref. [60] for a phase-mismatched SHG interaction.

Of the two idler pulse components, the first, main component travels with the signal in time until its constituent spectral components (frequency Ω) are amplified at the corresponding phase-matched points $z_{pm}(\Omega)$ (i.e. the points where $\Delta\beta(z,\Omega) = 0$). The second component travels at the idler group velocity, and hence walks off of the signal pulse, and then experiences an essentially separate OPA interaction, based on the same set of phase-matched points $z_{pm}(\Omega)$.

The resulting amplified output of both waves involves multiple pulse components: the main part, associated with the first pulse component described above, and pre- or post pulses, which originate from the secondary idler pulse component. The corresponding spectrum has ripples, associated with these multiple, delayed components [2]. Apodization serves to suppress the secondary pulse component, by optimally matching the input eigenmodes of the device to the input conditions (finite seeded wave, zero unseeded wave) [8]. However, in practice, apodization is never perfect in a device with $d(z)/d_{33} = \pm 1$, and so there is always at least a small secondary pulse component generated at the device input.

In the absence of pump saturation, the gain for each pulse component is essentially the same (except for slight changes due to the time-dependent intensity of the pump). However, with saturation, the weaker, unwanted pulse component can experience higher gain, since it saturates its temporal region of the pump less than the main pulse. The resulting pulse components cause an increased and unwanted spectral ripple. The use of a chirped seed pulse can either exacerbate or, when properly arranged, completely resolve this problem. We discuss the chirped-pulse case in the following subsection.

7.2. *Influence of saturation and input pulse chirp*

To understand the combined effects of GVM, saturation, and pulse chirp, it is useful to first consider the characteristic velocities involved in the chirped-pulse interaction.

There are the temporal walk-off rates associated with the carrier frequencies of the three waves, determined by their group velocities. There is in addition an "amplification wave-front" which corresponds to the delay of the seed spectral component $\Omega_{pm}(z)$ being amplified at position z (subscript *pm* indicates "phase-matched"). We denote this delay as $\tau_{sw}(z,\Omega_{pm}(z))$, where $\tau_{sw}(z,\Omega)$ is the group delay of frequency Ω and "sw" denotes seeded wave. Note that this delay is related to the instantaneous frequency $\Omega_{\text{inst}}(z,t)$ by $\Omega_{\text{inst}}(z,\tau_{sw}(z,\Omega)) = \Omega$. Note also that in

#205795 - $15.00 USD Received 4 Feb 2014; revised 3 Apr 2014; accepted 8 Apr 2014; published 15 Apr 2014

this section we will use Ω and Ω_{pm} to refer to frequency shifts of the *seeded* wave with respect to its carrier frequency ω_{sw}, which is equal either to ω_i or ω_s. The unseeded wave has carrier frequency $\omega_{uw} = \omega_p - \omega_{sw}$.

As well as an amplification wave-front, there is also a "secondary wave-front" related to the accumulated delays of the spectral components of the secondary (unwanted) pulse component which is generated in the envelope of the unseeded wave at the input to the grating, as described above in subsection 7.1.

In order for the secondary pulse to not saturate the pump before the main components are able to, it is necessary that these components travel at an opposite group velocity, relative to the pump, compared to the amplification wave-front. In the following, we quantify this constraint. In Fig. 7 and corresponding movies (Media 1 and Media 2), we illustrate the dynamics involved for an example signal-seeded configuration involving positive or negative chirp on the signal pulse. In the following paragraphs, we quantify the relevant processes and arrive at constraints for system design.

Each spectral component of the secondary pulse propagates at the corresponding group velocity of the material, given by $v_{uw}(-\Omega)^{-1} = (\partial k_e/\partial\omega)|_{\omega=\omega_{uw}-\Omega}$. The total group delay of these spectral components is determined by this group velocity and also by their initial group delays at the input to the grating, which are in turn determined by the chirp of the input (i.e. seeded) pulse. The secondary wave-front can therefore be expressed as:

$$\tau_{uw,\mathrm{eff}}(z) = \tau_{uw}(0, -\Omega_{pm}(z)) + v_{uw}(-\Omega_{pm}(z))^{-1} z, \tag{30}$$

where the initial group delay spectrum of the secondary pulse satisfies $\tau_{uw}(0,-\Omega) = \tau_{sw}(0,\Omega)$, where $\tau_{sw}(0,\Omega)$ is the group delay spectrum of the seeded pulse, determined by its chirp. We can now introduce an effective group velocity of the secondary wave-front given by

$$\begin{aligned} v_{uw,\mathrm{eff}}(z)^{-1} &= \frac{d\tau_{uw,\mathrm{eff}}}{dz} \\ &= \frac{1}{v_{uw}(-\Omega_{pm}(z))} + \left(\left.\frac{d\tau_{sw}(0,\Omega)}{d\Omega}\right|_{\Omega=\Omega_{pm}} - \beta_{uw,GVD}(-\Omega_{pm}(z))z \right) \frac{d\Omega_{pm}}{dz}. \end{aligned} \tag{31}$$

where we use $\beta_{j,GVD} = d(1/v_j)/d\Omega$ to denote the GDD coefficient of wave j (related to group velocity dispersion, GVD), and $\beta_{j,GDD} = d\tau_j/d\Omega$ to denote the GDD itself. Next, we consider the amplification wave-front group velocity, $v_{amp}(\Omega)$. The QPM chirp and material dispersion determine the rate at which the phase-matched frequency of the seeded wave changes with position, according to the implicit relation $\Delta k_0(\Omega_{pm}(z)) - K_g(z) = 0$. Hence, Ω_{pm} satisfies

$$\begin{aligned} \frac{d\Omega_{pm}}{dz} &= \frac{dK_g}{dz}\left.\frac{d\Delta k_0}{d\Omega}\right|^{-1}_{\Omega=\Omega_{pm}} \\ &= -\Delta k'(z)\delta v_{uw,sw}(\Omega_{pm})^{-1} \end{aligned} \tag{32}$$

where $\Delta k' \equiv \partial\Delta\beta/\partial z = -dK_g/dz$, and $\delta v_{uw,sw}(\Omega) \equiv d\Delta k_0/d\Omega = (v_{uw}(-\Omega)^{-1} - v_{sw}(\Omega)^{-1})$. From the change in phase-matched frequency versus position and the (position-dependent) pulse chirp of the seeded wave, we can calculate the group velocity of the amplification wave-front. We thereby arrive at

$$\begin{aligned} v_{amp}(z)^{-1} &= \frac{d}{dz}\left(\tau_{sw}(z,\Omega_{pm}(z))\right) \\ &= \frac{1}{v_{sw}(\Omega_{pm}(z))} - \left(\left.\frac{\partial\tau_{sw}}{\partial\Omega}\right|_{\Omega=\Omega_{pm}(z)} + \beta_{sw,GVD}(\Omega_{pm}(z))z \right) \frac{\Delta k'(z)}{\delta v_{uw,sw}(\Omega_{pm}(z))}. \end{aligned} \tag{33}$$

#205795 - $15.00 USD Received 4 Feb 2014; revised 3 Apr 2014; accepted 8 Apr 2014; published 15 Apr 2014

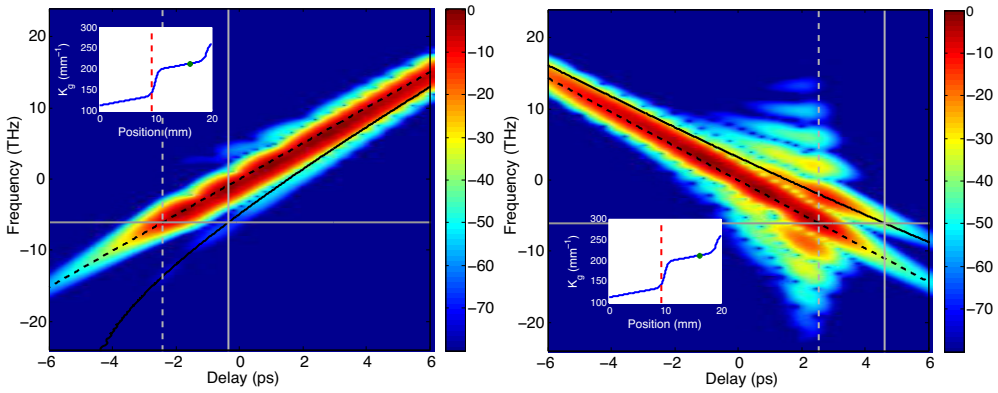

Fig. 7. Illustration of group velocity walk-off effects in saturated-pump OPCPA. (a) Negative signal GDD (Media 1), (b) Positive signal GDD (Media 2). The figures and movies show the evolution of cross- frequency resolved optical gating (FROG) spectrograms (dB scale; 400 fs gate pulse) of the unseeded wave (in this case, the long-wavelength idler) as it propagates through the QPM grating. The pump pulse is 12 ps long and the 1.55-μm signal input is stretched from 30 fs to 6 ps with pure second-order phase. The z-dependence of K_g is shown in the inset. The first $\sim$10 mm of the grating is a highly phase mismatched region, added to illustrate the relevant dynamics: this region allows the secondary pulse to propagate away from the main pulse, making it easier to distinguish; in a practical device, this region would not be included. The current position in the grating is marked for each frame.

Several curves are included in the main plot to highlight important features. The dashed black line shows the group delays of the main pulse, determined by the input chirp and propagation of the seeded pulse. The solid black line shows the group delays of the secondary pulse. The horizontal grey line shows the local phase-matched frequency. The dashed vertical line shows the amplification wave-front, corresponding to velocity $v_{amp}(z)$ [see Eq. (33)]. The solid vertical line shows the secondary wave-front, travelling at velocity $v_{uw,\mathrm{eff}}(z)$ [see Eq. (31)]. The intersection of the horizontal and vertical lines indicate the points of the pulse components which are currently phase-matched.

Distortions occur when the amplification wave-front passes through temporal regions of the pump which have already been depleted by the secondary pulse. This case is seen in (b) for positive signal GDD. Due to the highly amplified secondary pulse, there are two spectral regions of the signal and idler overlapped with each temporal region of the pump; cross-talk between these multiple pulse components lead to generation of additional spectral components, as seen in the image displayed for (b). In (a), the secondary wave-front 'lags behind' the amplification wave-front, so the secondary pulses are amplified less, and the output spectrogram quality is much higher.

The terms in Eqs. (31) and (33) dependent on $\tau_{sw}(0,\Omega)$ can be simplified by noting that $d\tau_{sw}(0,\Omega)/d\Omega = \beta_{sw,GDD}(\Omega)$, which is the frequency-dependent group delay dispersion of the seeded wave.

Given $v_{uw,\mathrm{eff}}(z)$ and $v_{amp}(z)$, the criteria introduced above for the secondary pulse components to not interact with temporal regions of the pump before the main pulse can be quantified:

$$\left(v_{uw,\mathrm{eff}}(z)^{-1} - v_{amp}(z)^{-1}\right)\left(v_{amp}(z)^{-1} - v_p^{-1}\right) < 0. \tag{34}$$

To interpret this equation: if $(v_{amp}^{-1} - v_p^{-1}) > 0$, the amplification wave-front moves from the leading edge of the pump to the trailing edge. We then want the secondary wave-front to be

#205795 - $15.00 USD Received 4 Feb 2014; revised 3 Apr 2014; accepted 8 Apr 2014; published 15 Apr 2014

closer in time to the leading edge of the pump than the amplification wave-front, so that it is temporally overlapped with pump components which have already been partially depleted. Thus, we need $v_{uw,\mathrm{eff}}^{-1} < v_{amp}^{-1}$, so that the secondary wave-front accumulates less delay with position. An analogous argument applies if both signs are reversed.

A convenient form for Eq. (34) results if we suppress dependencies of the various quantities on position z and frequency $\Omega_{pm}(z)$, and neglect group delay dispersion accumulated by both envelopes *within* the crystal, i.e. neglecting $\beta_{j,GVD}$. Equation (34) can then be re-written as

$$\beta_{sw,GDD}\Delta k' > \left(v_{uw}^{-1} - v_{sw}^{-1}\right)\left(v_{sw}^{-1} - v_{p}^{-1}\right). \tag{35}$$

Even further simplification of this inequality is possible in the case of a large enough GDD that the magnitude of the left hand exceeds that of the right hand side. In this case, we simply require that $\beta_{sw,GDD}\Delta k' > 0$. Since we found in section 6 that for the mid-IR OPCPA case under consideration, $\Delta k' < 0$ is required, Eq. (35) reduces, for strongly chirped pulses and gratings, to $\beta_{sw,GDD} < 0$, i.e. the seeded wave (whether the signal or idler) should have negative GDD.

In our OPCPA system [Fig. 1], the final idler output is compressed with bulk sapphire, which has a negative GDD coefficient in the 3- to 4-μm range. Prior to compression, the idler therefore has positive GDD. In the OPCPA stages, the even-orders of dispersion of the generated wave acquire a sign flip with respect to those of the seeded wave (note that the odd orders do not acquire such a sign flip). The seeded signal wave prior to OPA3 must therefore have negative GDD, in accordance with Eq. (35). We designed the silicon prism pair and 4-f pulse shaper seed-stretching system depicted in Fig. 1 so as to obtain such a negative signal GDD while also being able to compensate for higher order dispersion terms of the generated idler wave.

In addition to the somewhat subtle points discussed so far in this section, there is also a more obvious constraint based purely on temporal overlap of the pulses. To remain overlapped with the pump throughout the grating, using Eq. (15) to find the grating length L as a function of γ_{p0} and $\Lambda_{R,p}$, the pump duration should satisfy

$$\tau_p \gg \left(\frac{\Delta k_{\mathrm{OPA}}}{\gamma_{p0}^2 c} + \frac{4}{\gamma_{p0} c}\right)\delta n_g \Lambda_{R,p}, \tag{36}$$

where δn_g is a characteristic group index difference, corresponding to the largest group index minus the smallest group index involved in the three-wave interaction. With this inequality, the required pump duration can be estimated given the required gain and bandwidth. The minimum required pump pulse duration is obtained when the pump intensity equals the damage threshold, although this damage threshold is also a function of the pump duration.

To emphasize the results of this section: while the dynamics we have considered in Fig. 7 are quite complicated, the constraint imposed on OPCPA system design is very simple, requiring only that in any OPA stage with significant depletion of part of the pump temporal profile, the seed should have the appropriate sign of GDD (negative in the case of our system, since we also require $\Delta k' < 0$). The pulse stretching / compression can then be arranged with this constraint in mind, in addition to standard linear-optical considerations.

8. Summary and conclusions

8.1. Summary of OPCPA design constraints

In this subsection, we summarize the design constraints developed throughout this paper. One aspect of these constraints is that they apply to both the OPCPA system as well as the individual QPM devices, so it is important to design both at the same time.

To obtain sufficient gain, the factor $\Lambda_{R,p} = \gamma_p^2/|\Delta k'|$ must be large enough; the corresponding gain is given by Eq. (9). The actual gain and saturation in individual stages when using

#205795 - $15.00 USD Received 4 Feb 2014; revised 3 Apr 2014; accepted 8 Apr 2014; published 15 Apr 2014

Gaussian beams and non-flat-top pulses must be calculated numerically using e.g. Eq. (1). The amplification bandwidth is given by Eq. (15) or more generally by Eq. (10). For a given bandwidth and gain, there are two equations for the three quantities γ_p, L, and $\Delta k'$. Avoiding $\chi^{(3)}$ and $\chi^{(3)}$-like processes, which typically scale with the intensity-length product (but also depend in some cases on the temporal structure of the waves) is also important. We considered such processes in appendix A.

The peak signal-idler coupling rate γ_p [Eq. (11)] is in addition constrained by the damage threshold, which is a function of duration (for peak-intensity related damage), and also by the thermal load on the crystal (for average power- and intensity- related damage). The grating length L is also constrained by fabrication, but lengths of ~ 50 mm are available, so this constraint can usually be ignored for OPCPA. The QPM crystal aperture along the c-axis can be quite narrow (e.g. ~ 3 mm available commercially with good domain quality). Nonetheless, samples of up to 10 mm aperture have been demonstrated [61], as well as rotated-cut wafer poling supporting wafer-sized beams [62], so QPM devices can be scaled to high powers and energies. Wider gratings and elliptical beams may be necessary sometimes for power scaling. In our case we used 1x3 mm gratings, but 2x2 mm gratings would be a natural alternative.

Achieving high conversion efficiency in a single high-gain OPA stage is difficult and requires the parametric interaction to be driven very strongly, as indicated by Fig. 2. Use of a pump which is too strong will result in excess noise amplification and other, unwanted effects such as those discussed in sections 4, 5 and 6 and appendix A. Keeping a moderate pump intensity, corresponding for example to a peak $\Lambda_{R,p}$ of $1.5 < \Lambda_{R,p} < 3$ means that multiple OPA stages must be used in order to achieve good conversion efficiency in the final stage. Based on these considerations and the properties of our pump source, we split our OPCPA system up into two pre-amplifier stages followed by the power amplifier. Previously [4, 5], only a single strongly-driven pre-amplifier was used.

Splitting the power amplifier into two parts and re-using the same pump, as we did for the pre-amplifier stages, would be a promising approach, since in this way the first power amplifier stage has (approximately) the same pump energy as the final stage, so a large ρ can be obtained in the final stage without very high saturation in the penultimate stage. To be able to re-use the pump in this way, its spatial and temporal properties must not be too heavily distorted in the penultimate stage; these properties are related to saturation effects and the QPM grating quality.

Imperfections in the QPM grating, in particular RDC errors, lead to parasitic SHG and TPA, and it is likely that these place limitations on the largest γ_p which we can use in practice before the onset of beam fanning due to photorefractive effects. Minimizing these RDC errors will be an important step for using larger γ_p without beam distortions and with less risk of crystal fracture. We estimate $\sigma_z \sim 0.4\ \mu$m for our present devices based on the generated green light. Evaluation of the RDC errors and minimizing them (to the extent possible given available fabrication technology) is likely to be important in optimizing system performance, particularly when using the same part of the pump for multiple stages.

Keeping a small-to-moderate level of group velocity mismatch between the waves relative to their durations imposes a further constraint, given by Eq. (36). Minimizing GVM will generally favor operation at the maximum intensity for a given pump duration and repetition rate (this maximum may correspond to a reversible onset of beam distortions or to irreversible damage of the crystal). Minimizing GVM is not necessarily a very strong constraint, however. With $\gamma_p = \gamma_{\max}$, the other nominal design quantities $\Delta k'$ and L of each stage can be determined. The use of a linear chirp is not required: shaping of the gain spectrum is possible, as described in Ref. [12] for OPCPA as well as other parametric mixing configurations. Once a nominal grating profile is chosen, suitable apodization profiles must be appended in order to achieve as clean a gain spectrum as possible. This aspect of the design, as well as a detailed discussion of the

#205795 - $15.00 USD Received 4 Feb 2014; revised 3 Apr 2014; accepted 8 Apr 2014; published 15 Apr 2014

underlying three-wave mixing process, was given in [8].

In terms of system constraints, the most important is likely the pump peak power constraint given in Eq. (24) (in the context of gain-guided non-collinear mode suppression), since this indicates the appropriate pump sources. For example, consider a system with a single pump beam which is then split into multiple parts to pump the different stages. With $P_{pk}/\Lambda_{R,p}^2 > 0.5$ MW [comparable to Eq. (25)], using $\Lambda_{R,p} = 2.5$, and using 10% of the total pump to drive one or more pre-amplification stages, one arrives at $P_{pk} > 30$ MW. To satisfy the constraint by a factor of $\sim$2 safety margin, one would need $P_{pk} > 60$ MW. Fortunately, such peak powers are now readily achievable in a variety of laser systems, but this constraint is still important in scaling to high repetition rates. In our system, we re-used the OPA1 pump for OPA2, and operated at 50 kHz in order to achieve a sufficient safety margin in the pre-amplifiers given the peak power available from our pump source.

Given operation at the damage threshold, characterized by $\gamma_{\max}(\tau_p, f_{rep})$ (i.e. assuming a damage threshold, and corresponding maximum signal-idler coupling rate, which is a function of both the pump duration and its repetition rate), the GVM constraint Eq. (36) can turn the above peak power requirement into a pulse energy requirement.

To avoid unwanted coincidentally phase-matched processes in the OPA stages, it is important to inspect the relevant phase-matching maps, taking into account the range of QPM periods required for the desired interaction. For the mid-IR OPCPA case we focused on in this paper, this consideration imposed the constraint $\Delta k' < 0$. Note that with our definitions, $\Delta k' = \partial \Delta k/dz = -dK_g/dz$, so $\Delta k' < 0$ implies an increasing $K_g(z)$ and hence a decreasing QPM period versus position in the grating. Note also that if $\Delta k_0(\Omega)$ was negative for some mixing configuration, then the residual QPM phase-mismatch would be $(\Delta k_0 + K_g)$ rather than $(\Delta k_0 - K_g)$; one would then have $\Delta k' = +dK_g/dz$w.

The presence of GVM between the waves and the use of chirped pulses and gratings can lead to unwanted temporal effects, as discussed in section 7. These effects can be avoided by satisfying Eq. (34), which will often reduce to Eq. (35) in practice. For our case, this constraint together with the above $\Delta k'$ constraint meant a negative chirp on the signal was needed. This chirp resulted in a positive idler chirp, requiring a negative-GVD material (such as sapphire) for bulk compression of the generated idler. As such, the pulse stretching/compression should be arranged with OPCPA constraints in mind. We use general ray-tracing procedures for evaluating and optimizing linear-optical pulse chirping and compression strategies [63], incorporating both the constraints discussed here and the spectral phase imposed onto the generated wave in the chirped QPM structure [64]. We note, also, that the pulse-distortion effects discussed in section 7 may become negligible for very long ($\gg$ 10 ps) pump pulses.

The above constraints, in addition to more "standard" OPCPA considerations, have proven sufficient for development of our OPCPA system. In some cases, they represent subtle issues not previously discussed or quantified in the context of chirped-QPM OPCPA design. Deciding on specific beam sizes, distribution of gains between stages, arrangement of pulse chirping and compression stages, and other experimental aspects, can be facilitated by (1) the comprehensive analytical design equations and constraints we developed here, (2) more detailed numerical calculations based on a generalized coupled-envelope model [Eqs. (1) and (4)], accounting for all propagation effects including diffraction, dispersion, nonlinearities, presence of multiple OPCPA stages, and so on (which is beyond the scope of this paper), and (3) optimization of performance experimentally, guided by (1) and (2).

More generally, it is important to decide on appropriate pump sources (based on criteria such as cost/complexity, wavelength, pulse energy, duration, and repetition rate) and seed sources (based on criteria such as wavelength, bandwidth, energy, stability, and spectral quality, as well as cost/complexity). These considerations will continue to evolve as the relevant laser

#205795 - $15.00 USD Received 4 Feb 2014; revised 3 Apr 2014; accepted 8 Apr 2014; published 15 Apr 2014

technologies improve and become more available, and so we have not focused on them here.

8.2. Conclusions

The design and operation of chirped QPM devices can be subtle and complex. Initially unexpected effects can arise and amplify noise, distort beam and/or pulse profiles, or even damage the nonlinear crystals. In this paper, we have presented a systematic analysis of the design of OPCPA systems based on these devices, identifying several important constraints beyond those usually present for OPCPA. While the underlying spatio-temporal dynamics can be complex, the resulting design constraints, summarized above in subsection 8.1, are often comparatively simple. For example, imposing particular signs on the grating and pulse chirps, necessitating a pump with sufficient peak power, placing limits on the local disorder of the QPM grating domains, and indicating the number of OPA stages required in the system.

As a result, our analysis provides a roadmap for development of chirped QPM OPCPA systems in the lab while avoiding the subtle unwanted effects which the combination of pulse and grating chirp can introduce. So far, this enabled us to obtain almost a factor-of-2 improvement in pulse duration, resulting in our latest 41.6-fs mid-IR OPCPA result [1]. The constraints we have developed here reveal several important steps in further advancing QPM OPCPA towards fewer-cycle pulses, higher energies, and new wavelength regions, while pumping with power-scalable 1-μm laser sources and maintaining simple and compact experimental setups.

There is no relevant limit to the achievable bandwidth with respect to phase-matching, except for the crystal transparency window. Therefore, understanding the physics of the nonlinear processes involved (including the role of multiple, potentially competing nonlinearities), and evaluating that physics in the context of system design, is the key to making use of the broadband phase-matching which QPM technology supports. The general frequency-domain multiple-envelope model we introduced will be useful in modelling a wide variety of parametric interactions, especially when augmented by $\chi^{(3)}$ effects. Our results will also make it possible to evaluate the feasibility of exploiting engineered QPM in emerging far-IR materials, for example to achieve OPA and OPCPA in orientation-patterned GaAs [65, 66].

Beyond OPCPA, our results apply to chirped QPM devices in general. In particular, for DFG and SFG interactions, especially when both of the input waves are intense, most of the constraints we have developed will also apply directly or with minor modifications. Furthermore, the spatial, spectral, and temporal effects discussed in sections 4, 6, and 7, respectively, will apply to media with spatially inhomogeneous phase-matching conditions, not just chirped QPM media, and thus our results have broad applicability to designing and understanding strongly-driven parametric systems in general.

A. Justification of a model based on $\chi^{(2)}$ effects

There are a number of $\chi^{(3)}$ and $\chi^{(3)}$-like processes which can also influence the desired OPCPA interaction, beyond the $\chi^{(2)}$ dynamics predicted by the nonlinear polarization in Eq. (4). In this appendix, we consider the significance of some of these neglected $\chi^{(3)}$ effects in order to help justify the use of the simplified $\chi^{(2)}$-based model in Eqs. (1) and (4).

Relevant processes include the (near-)instantaneous electronic susceptibility $\chi_E^{(3)}$ and stimulated Raman scattering (SRS), which we denote by a frequency dependent susceptibility $\chi_R^{(3)}(\Omega)$. Furthermore, optical rectification (OR)-related processes can also occur: specifically, the optical field can generate quasi-phase-matched counter-propagating THz waves, which in turn can couple different spectral regions of the optical field together [67, 68]. These latter effects have been quantified in the context of singly resonant OPO operation [69, 70].

Absolutely calibrating the third-order susceptibilities in $LiNbO_3$ is challenging, owing for example to contributions from cascaded $\chi^{(2)}$ (even in bulk and with no QPM grating), as well

#205795 - $15.00 USD Received 4 Feb 2014; revised 3 Apr 2014; accepted 8 Apr 2014; published 15 Apr 2014

as non-instantaneous nonlinearities such as SRS. In [46], we attempted to calibrate these effects in the context of supercontinuum generation based on the measurements performed in [55], and arrived at an electronic susceptibility of $\chi_E^{(3)} = 5480$ pm^2/V^2 and a peak SRS susceptibility of $\chi_{R,pk}^{(3)} = 5230$ pm^2/V^2, together with a corresponding complex SRS response function. Here we use these values, but note that further, direct measurements of these quantities would be useful.

The corresponding pump SPM via $\chi_E^{(3)}$ is 0.75 rad for an intensity of 5 GW/cm^2 and a grating length of 11 mm. There is also a near-instantaneous SPM-like response from cascaded quadratic nonlinearities, originating from all Fourier orders far from phase-matching. Such contributions influence both the pump SPM, the calibration of $\chi_E^{(3)}$, and also the different nonlinear phase shifts incurred by the signal and idler waves. Furthermore, there is significant uncertainty in the above phase from $\chi_E^{(3)}$. If one just uses the n_2 reported in [55] to determine $\chi_E^{(3)}$ (without accounting for other nonlinear processes), the SPM predicted is ≈ 3.4 times smaller.

The maximum SRS gain supported is comparable to the B-integral from $\chi_E^{(3)}$ owing to their comparable susceptibilities, but its influence on the pulse spectrum can be expected to be minor, since the strongest Raman peak is at ≈ 19 THz, which is well outside the range of spectral components supported by the *intensity* of a few-ps pulse. Nonetheless, SRS effects may not be vanishingly small in OPA3, in which the signal and idler intensities grow enough to substantially saturate the pump, because our pulses exhibit significant spectral structure. Such structure maps to temporal structure for a chirped pulse and will thus broaden the Fourier spectrum of the chirped pulses' intensity, thereby sampling a broader range of the Raman spectrum (which also has peaks at lower frequencies such as 7.6 THz).

The OR-related sources of pulse distortion lead to SRS-like effects, but they depend on the QPM grating structure. Specifically, phase-matching for counter-propagating THz waves is governed, approximately, by $\Delta k_T(z,\Omega) = (n_T + n_g)\Omega/c - K_g(z) = 0$, where n_T is the THz refractive index (~ 5.2 for $LiNbO_3$ [71]), and n_g is the optical group index (≈ 2.2 at 1 μm). This relation yields a phase-matched THz frequency Ω_{pm} satisfying $\Omega_{pm} = K_g(z)c/(n_T + n_g)$. For 1-$\mu$m-pumped mid-IR OPCPA in MgO:$LiNbO_3$, the QPM periods are around 30 μm, which yields a frequency of 1.35 THz, respectively.

The bandwidth of the generated THz waves depends on the driving field, but in the limit of a short intensity profile of the pulse, the THz field scales according to $\tilde{A}_T(\Omega) \propto \Omega/[\alpha_T(\Omega)/2 + i(n_T + n_g)(\Omega - \Omega_{pm})/c]$, where α_T is the frequency-dependent THz absorption coefficient. This Lorentzian-like response has a relatively narrow bandwidth, determined by the absorption and index mismatch parameters according to $\Omega_{BW} = \alpha_T(\Omega_{pm})c/[2(n_T + n_g)]$. For the counter-propagating 1.35 THz case considered above, $\Omega_{BW} = 2\pi \times 0.014$ THz. The effective susceptibility seen by the optical field is given by

$$\chi_T^{(3)}(\Omega) = \frac{16 d_T^2}{3 n_T c} \frac{\Omega}{\alpha_T + i(n_T + n_g)(\Omega - \Omega_{pm})}. \tag{37}$$

In the context of narrow-band OPOs, this susceptibility can also be viewed as a THz OPA process [69]. Assuming $d_T = 2/\pi \times 152.4$ pm^2/V^2 [71], Eq. (37) yields a peak of 125.6×10^3 pm^2/V^2, i.e. much greater than the $\chi_E^{(3)}$ and $\chi_R^{(3)}$ responses discussed above. This large effective susceptibility helps explain the susceptibility of cw-pumped OPOs to this nonlinearity. In the context of OPCPA, the distortion of the pulse is weak for pulses with narrow-band intensity Fourier spectra; if the pulses are short enough (or have a sufficiently modulated structure) to have intensity spectra approaching Ω_{BW}, the significance of the resulting pulse distortion can be (over-)estimated in the same manner as a calculation for the small-signal SRS gain (based on the pump intensity and the effective third-order susceptibility), but multiplying by $\Omega_{BW}/\Omega_{pm} \approx 0.01$. This calculation yields an an "effective coupling" due to OR of ~ 0.36.

#205795 - $15.00 USD Received 4 Feb 2014; revised 3 Apr 2014; accepted 8 Apr 2014; published 15 Apr 2014

While this coupling is not vanishingly small, the use of a chirped QPM grating strongly smears out the THz response, since $K_g(z)$, and hence $\Omega_{pm}(z)$, varies with position in the grating. Furthermore, the actual coupling obtained in practice will be much weaker than the above estimation, because the signal and idler have lower intensity than the pump, and the pump can be very narrow-band compared to Ω_{pm} (if its pulse duration is long enough). If in addition the signal and idler spectra are slowly-varying and the pulses are chirped to comparable duration to the pump, there will be very little coupling to the THz wave. It should also be noted, however, that the above treatment of coupling to THz waves is by no means comprehensive: for example, we have not considered any effects involving phonon-polariton dynamics or the possible influence of periodic poling in the ferroelectric crystal on such processes [72].

Based on the above discussion, we expect that $\chi^{(3)}$ effects are minor, but not completely negligible in all cases. Such effects should thus be kept in mind when designing and characterizing OPCPA systems, including SRS-like processes in addition to B-integral considerations. A greater knowledge of the relevant third-order nonlinear coefficients for $LiNbO_3$ will also be useful in order to more reliably quantify these issues.

B. Definitions and important quantities

This paper involves many definitions and symbols, and draws on various results. For ease of reference, the tables 1-4 summarize the important quantities defined in the main text.

Table 1. Summary of basic quantities defined in the paper

Symbol	Description	Defined
$\hat{L}_j$	Diffraction and dispersion operators	Eq. (2)
A_j	Electric field envelopes	Eq. (3)
$P_{NL,j}$	Nonlinear polarizations	Eq. (4)
$X_{k,jl}$	Interaction coefficients ($=0$ or $=1$)	Eq. (5)
$\Delta k_{j,kl}$	Phase-mismatches for various carrier frequencies	Eq. (6)
$\Delta\beta(z)$	Carrier-frequency quasi-phase-mismatch for OPA	Eq. (8)
$\Delta k'$	QPM chirp rate, $\Delta k' = \partial\Delta\beta/\partial z = -dK_g/dz$	After Eq. (9)
$\Delta k_0(\Omega)$	Frequency-dependent phase-mismatch (OPA)	Eq. (12)
$\mathbf{\Delta k}$	Vector phase mismatch	Eq. (17)
$\phi_G(z)$	Accumulated QPM grating phase, $\int_0^z K_g(z')dz'$	Eq. (7)
$K_g(z)$	Local QPM grating k-vector	Eq. (7)
$D(z)$	Local QPM grating duty cycle	Eq. (7)
$d(z), d_m$	Absolute & normalized nonlinear coefficients	Eq. (7)
d_{eff}	Effective nonlinear coefficient, $d_{\text{eff}} = d_{33}\bar{d}_1$	Eq. (8)
γ_p	Signal-idler coupling rate (OPA); $\propto \lvert A_p\rvert$	Preceding Eq. (9)
γ_{p0}	Peak of γ_p (when γ_p varies vs. space or time)	See Eq. (15)
γ_s	Idler-pump coupling rate (SFG/DFG); $\propto \lvert A_s\rvert$	Preceding Eq. (9)
$\gamma_{\max}$	Max. γ_p possible (at damage threshold)	

#205795 - $15.00 USD Received 4 Feb 2014; revised 3 Apr 2014; accepted 8 Apr 2014; published 15 Apr 2014

Table 2. Summary of basic chirped QPM OPCPA related quantities

Symbol	Description	Defined
G_s	$\sim \exp(2\pi\Lambda_{R,p})$; Signal gain (no pump depletion)	Eqs. (9) and (10)
z_{pm}	Frequency-dependent phase-matching point	Eq. (13)
L_{deph}	$2\gamma_p/\lvert\Delta k'\rvert$; half the distance over which gain occurs	Eq. (14)
Δk_{OPA}	$\lvert\Delta k'\rvert L - 4\gamma_{p0}$; OPA gain bandwidth (k-space)	Eq. (15)
Δk_{BW}	$\lvert\Delta k'\rvert L$; bandwidth of QPM grating (k-space)	Eq. (15)
$\Lambda_{R,p}$	$\gamma_p^2/\lvert\Delta k'\rvert$; Gain factor (determines small-signal gain)	Eq. (16)
$\Lambda_{R,s}$	$\gamma_s^2/\lvert\Delta k'\rvert$; Pump depletion factor for SFG/DFG	Subsection 3.3
ρ	Ratio of input signal and pump photon fluxes	Subsection 3.3
η	Pump depletion (output / input pump intensity)	Subsection 3.3
L	QPM grating length	

Table 3. Summary of definitions used primarily in sections 4, 5, and 6.

Symbol	Description	Defined
ξ_p	Pump confocal parameter	See Eq. (16)
L_g	Gain length	$L_g = \gamma_{p0}^{-1}$
L_{wo}	w_p/θ_{is}; Spatial walk-off length ($1/e^2$ radius w_p)	Subsection 4.2
θ_{is}	Geometric mean phase-matching angle	Eq. (20)
$\theta_{is,\max}$	Maximum of θ_{is} (vs. wavelength)	Eq. (23)
Γ	Gain-guided mode gain rate ($\Gamma \leq \gamma_{p0}$)	Fig. 3(a)
$\tilde{g}_{\mathbf{z}}(k)$	Spatial Fourier transform of QPM grating	Eq. (26)
σ_z	Standard deviation of QPM RDC errors	See Eq. (26)
N	Number of domains in the QPM grating	Eq. (26)
l_D	Half the QPM period	Subsection 5.1
U_{SH}	Generated pump SHG (RDC errors)	Eq. (27)
U_{TPA}	Two-photon-absorbed pump SHG (RDC errors)	Eq. (28)
β_{TPA}	Two-photon absorption coefficient	Eq. (28)
d_{OPA}	Nonlinear coefficient for OPA	Eq. (27)
d_{SHG}	Nonlinear coefficient for pump-SHG	Eq. (27)
$\Delta k_{si}^{(DFG)}$	Phase-mismatch for signal-idler DFG	Eq. (29)

Table 4. Summary of definitions used primarily in section 7.

Symbol	Description
$v_{sw}(\Omega)$	Group velocity of the seeded wave
$v_{uw}(\Omega)$	Group velocity of the unseeded wave
$v_{amp}(z)$	Effective velocity of the amplification wavefront
$\tau_{sw}(z,\Omega)$	Group delay spectrum of the seeded wave
$\tau_{uw}(z,\Omega)$	Group delay spectrum of the unseeded wave
$\tau_{uw,\text{eff}}(z)$	Effective delay of the secondary wavefront
$v_{uw,\text{eff}}(z)$	Effective velocity of the secondary wavefront
$\beta_{j,GVD}(\Omega)$	GDD coefficient of wave j ($j = sw$ or $j = uw$)
$\beta_{j,GDD}(z,\Omega)$	GDD of wave j ($j = sw$ or $j = uw$)
$\Omega_{pm}(z)$	Phase-matched seeded-wave frequency at position z
$\Omega_{\text{inst}}(z,t)$	Instantaneous seeded-wave frequency
$\delta v_{uw,sw}(\Omega)$	GVM coefficient between the seeded and unseeded waves

#205795 - $15.00 USD Received 4 Feb 2014; revised 3 Apr 2014; accepted 8 Apr 2014; published 15 Apr 2014

Acknowledgments

This research was supported by a Marie Curie International Incoming Fellowship within the 7th European Community Framework Programme, by the Swiss National Science Foundation (SNSF) through grant #200020_144365/1, and by the U.S. Air Force Office of Scientific Research (AFOSR) under grants FA9550-09-1-0233 and FA9550-05-1-0180.

#205795 - $15.00 USD Received 4 Feb 2014; revised 3 Apr 2014; accepted 8 Apr 2014; published 15 Apr 2014